A high-resolution coupled ice-ocean model of winter circulation on the Bering Sea Shelf. Part I: ice model refinements and skill assessments

Scott M. Durski[1]

Alexander L. Kurapov[1,2]

Key points:

1. Enhancements made to a single-category ice model improved performance in simulating the Eastern Bering Sea in the winter of 2009-10.
2. Adjustments and corrections to the thermodynamics and modifications to the ice-ocean and atmosphere-ice drag formulations contributed to this improvement

[1] College of Earth, Ocean and Atmospheric Sciences, Oregon State University

[2] National Oceanic and Atmospheric Administration, Coast Survey Development Laboratory, Silver Spring, MD

Abstract

The Bering Sea Shelf transitions from ice-free to mostly ice-covered and back again over each winter. Sea ice coverage and the timing of ice melt play a critical role in determining shelf structure and consequently ecosystem response during the spring transition and summer. In this study, a 2-km resolution ocean model, which is based on the Regional Ocean Modeling System (ROMS) and was initially run and verified against a variety of observational data sources for summer 2009, is augmented with an ice model to study the coupled ice/ocean dynamics of the Bering Sea shelf from fall 2009 to summer 2010. Here we demonstrate that a single-category ice model is appropriate to describe seasonal evolution of the ice. Enhancements are made to the ice thermodynamic module and air/ice stress formulations to improve the match between the model and satellite microwave estimates of ice distribution and extent. The refined model accurately represents the timing and spatial extent of the spread of sea ice over the winter season as well as the ice retreat as it melts in spring and summer. Comparison with satellite products also suggests that the model captures the sea ice response on shorter temporal (~O(days)) and spatial scales (~O(20km)). The modification to the drag formulation for example, can improve the modeled sea ice distribution in response to wind events overall and in particular in polynya regions along the coastlines of the Seward and Chukotka peninsulas and St. Lawrence Island.

1 Introduction

Each fall and winter, sea ice spreads across the greater than 500-km wide Eastern Bering Sea shelf until spring melting returns the shelf to ice-free by summer. There is significant interannual variability in the timing of the advance and retreat and in the peak extent of the ice (Niebauer, 1983). Sea ice is produced locally, particularly in the shallower and more northern portions of the shelf and is transported southward and westward with prevailing winds to cover a large fraction of the shelf area in some years. Because most of the Bering Sea ice is in free drift (Reynolds et al., 1985), rather than land locked, unlike most Arctic ice in winter, throughout the season changes in winds cause considerable repositioning of the mass of sea ice causing the appearance and disappearance of polynyas on the various bordering coastlines and island shores. The timing of the melt-off relative to the annual solar cycle and the distribution of where melt occurs in part determines the ecological characteristics of the Bering Sea shelf in spring and summer (Ladd & Stabeno, 2012). Given its size and the significant spatial and temporal variability, developing a detailed understanding of shelf winter characteristics and dynamics is challenging.

In situ observations of ice and water characteristics on the Bering Sea shelf are limited. Visible satellite imagery provides details of ice distributions, but only intermittently as much of the shelf tends to be occluded by clouds for much of the winter. Even in the absence of clouds, satellite estimates of sea surface temperature, which are readily available for much of the global ocean, cannot be accurately estimated in the vicinity of sea ice. Microwave satellite imagery, which is much less impeded by clouds, provides a relatively accurate measure of the areal extent of sea ice with resolution as high as 5 km (Spreen et al., 2008). However, the instruments are limited in ability to quantify ice stresses, ice drift and thermodynamic fluxes between the ice, atmosphere and ocean. Recently techniques have been developed to measure sea surface height in ice-covered seas using satellite altimetry but so far these techniques apply to very coarse temporal and spatial resolution (Armitage et al., 2016). Information about the ocean beneath the ice mostly consists of point-data from long-term moorings that have been placed in Bering Strait (Woodgate et al., 2015) and at several locations on the shelf (Danielson et al., 2012; Stabeno et al., 2011b, 2011a) which necessarily leave much of the Eastern Bering Sea shelf undersampled. These factors point to the need for numerical models that can accurately represent the dynamics of the coupled sea-ice ocean system of the Eastern Bering Sea to provide a more complete picture than what is currently available.

Coupled ice-ocean models for the Bering Sea have been developed and utilized in a number of previous studies with some success. Single-category ice models distinguish only one ice thickness per model grid cell as opposed to more computationally expensive multiple-category ice models that find a distribution of ice properties in each grid cell based on ice thickness classes. Single category models have been incorporated into studies by Pritchard et al. (1990) for 5-7 day prediction of ice movement, by Clement et al.(2005) to study fluxes through the Bering Strait and by Clement-Kinney et al. (2009) who examined shelf-slope exchange processes. More recently, the model that is the predecessor to the one used in this study, namely the Regional Ocean Modeling System (ROMS) with the Budgell (2005) ice model implementation, was used to study interannual modes of variability in the Bering Sea by Danielson et al. (2011), and multidecadal biophysical variability by Hermann et al. (2016). More advanced multi-category ice models have also been applied to the Bering Sea by Wang et al. (2009) to study differences in winter and summer shelf circulation, by Hu and Wang (2010) to study the evolution of the "cold pool" and influence of tidal and wind/wave mixing, by Zhang et al. (2010) to study sea ice response to atmospheric and oceanic forcing in the Bering Sea, and by Zhang et al. (2012) to look at interannual variability in the ice dynamics and thermodynamics. Cheng et al. (2014) evaluated winter dynamics in the Bering Sea in the National Center for Atmospheric Research Community Earth Systems Model with comparison to satellite and in situ observations as well.

The studies mentioned above often present evidence that the incorporated ice models reproduce the ice coverage well enough to draw conclusions about interannual variability and/or average seasonal patterns, but detailed comparisons with observations within any particular winter season are omitted. Wang et al. (2009) display the seasonal cycle of sea ice area compared to satellite estimates averaged over 11 years, while Danielson et al. (2011) show a 40-year time series comparison of the same field, but without discussion of individual years. Cheng et al. (2014) compare ice concentrations at shelf mooring locations averaged over 19 years. Such average calculations are reasonable given the focus of such studies but leave many questions regarding intraseasonal variability in Bering Sea ice unanswered.

An argument can be made that incorporating ice thickness distribution within a grid cell and even floe size distribution is important in the marginal ice zone to accurately represent thermal exchanges and lateral melt rates (Zhang et al., 2015). At the same time, no study showed that transition from a single-category ice model to more computationally demanding multiple-category models is advantageous for the Bering Sea, e.g., providing improvement in the timing of the ice melt or ice concentration distribution as compared to the available satellite data. The present study demonstrates that with careful refinements, a single-category sea ice model coupled to a high-resolution ocean circulation model exhibits satisfactory performance when compared to the best available satellite estimates of sea ice concentration. As this work follows on an application of this same ocean model in a study of circulation in the Bering Sea in the ice-free season of June through October 2009 (Durski et al., 2016), Mauch et al., 2019), the coupled model performance is evaluated in the Eastern Bering Sea for the winter of 2009-2010. A single winter season is evaluated in detail with attention focused on the timing and the rate of seasonal freezing and melting as well as ice variability on intra-seasonal, weather-related temporal scales. As a starting point we choose the ice model that has been previously incorporated into a version of ROMS. It is the single-category ice model (Budgell, 2005) with elastic-viscous-plastic (EVP) rheology (Hunke & Dukowicz, 1997; Hunke, 2001) and ice thermodynamics based on the parameterization of Mellor and Kantha (1989). Earlier versions of this model have been used in Danielson et al. (2011) and Hermann et al. (2013). Despite some shortcomings, these earlier versions of the model formulation we start with, presented important steps in the development of the coupled ice-circulation modeling. The main goal of this manuscript is not to report computer code bug fixes, but to emphasize details of the atmosphere-ice-ocean material and heat exchange that are critical to the successful implementation of this, single category ice model.

The approach here was to carefully refine and optimize the code by progressively eliminating points of discrepancy between the model estimates of ice concentration and those obtained from satellite microwave radiometry. Danielson et al. (2011) noted a tendency in the precursor model for late fall freeze-up in the Bering Sea and notably delayed ice melt in the Spring. Our initial efforts to simulate the winter of 2009-2010 in the Bering Sea with the ice model component unaltered, exhibited similar inconsistencies. E.g., melting was delayed by about a month. So efforts for model refinement focused on matching the satellite-derived seasonal cycle in ice coverage, along with the spatial distributions of ice concentration, and the redistribution of ice concentration with wind events.

As is often the case in the implementation of complex algorithms, errors in coding and ambiguities in intention often only emerge as new scenarios are tested and different metrics are utilized. Consequently, model improvements discussed here fall into several categories including corrections to the code, additions to account for previously unconsidered model settings, and refinements to the physics and/or numerics. Ultimately two sets of changes to the parameterizations were settled on. One set involved only changes to the ice thermodynamics, while the other included additional modifications to the ice dynamics. While neither model solution is clearly superior by all metrics, the comparison of the two provides insight into the dynamics that drive the differences between the two.

The ocean model is described in section 2.1, the base ice model in section 2.2 and ice model refinements in Section 2.3. Section 3 presents comparisons of the improved ice model with satellite estimates of ice concentration on both seasonal and event time scales. A summary is presented in Section 4.

2 Model configuration and observational datasets

2.1 Ocean model

The ocean model setup utilized here follows directly from Durski et al. (2016) except where noted below. Simulations are performed using ROMS (http://www.myroms.org), a three-dimensional hydrostatic ocean model using terrain-following vertical coordinates. The model domain spans the region zonally from 178°E to 157°W and meridionally from roughly 50°N to 66.4°N [See Figure 1 in (Durski et al., 2016)]. The model grid is identical to that used in the Durski et al. (2016) study, with horizontal resolution of 2 km and 45 vertical levels.

The model is initialized on June 1st, 2009 using outputs from the global 1/12th° resolution Navy Hybrid Coordinate Ocean Model (HYCOM GLB[au]0.08 (Chassignet et al., 2007), http://www.hycom.org) melded with a Bering Ecosystem STudy ice-ocean Modeling and Assimilation System (BESTMAS) regional simulation solution (Zhang et al., 2010, 2012) for the Bering Sea shelf. The data-assimilative HYCOM model ensured accurate initialization of the large scale flow in the Bering Sea basin and North Pacific but did not provide accurate representation of the shelf stratification at the end of the melt-season. Melding with the BESTMAS shelf solution, which presumably captured the sea ice dynamics of the prior season more accurately, provided an initialization that allowed the model to more accurately capture the evolution of shelf stratification over the summer and fall of 2009. The melding was achieved by using the HYCOM fields in the deep basin, BESTMAS over the shelf and their weighted average in a buffer zone over the shelf slope providing smooth transition from one product to another.

Open boundary conditions for horizontal velocity, potential temperature, and salinity are specified as a combination of Orlanski radiation and nudging (on a 3 day time scale for inflow) to the 5-day time-filtered HYCOM global model solution. Different from in the original Durski et al. (2016) summer experiment, the model solution is also nudged towards HYCOM temperature and salinity in an approximately 75 km wide strip along the eastern, western and southern boundaries. This was found to be helpful in diminishing erroneous currents and ocean temperatures along the open boundaries over the longer integration time of this study. Over this same region increased horizontal viscosity and diffusivity are applied to damp erroneous boundary effects. Tidal forcing is applied at the model boundaries using four tidal constituents (K1, O1, M2, S2).

Our initial simulations exhibited an artificially intense Anadyr current flowing northward along the Chukotka Coast (Figure 1) during the late winter and spring months, resulting in transports through the Bering Strait that tended to be larger than those measured at moorings (Woodgate et al., 2015) (Figure 2; mooring positions shown in Figure 1). Considering the flow out of the northern boundary into the

Chukchi Sea to be proportional to that through the strait, the northern boundary conditions on SSH and northward depth-averaged velocity were "error-corrected". A time varying transport error was determined using the difference between a low-pass filtered Bering Strait section-averaged transport estimate from the moorings and from an uncorrected model simulation. This transport was converted into an equivalent geostrophic flow at the open boundary, where the boundary conditions for sea surface height and barotropic velocity were adjusted accordingly. These corrected values were applied in ROMS using Flather(1976) boundary conditions. This significantly reduced the error in the model estimate of the velocity at the mooring locations over the winter months and resulted in the slower Anadyr winter current.

Surface fluxes are parameterized using the COARE algorithm (Fairall et al., 2003) as implemented in the ROMS. Atmospheric near-surface temperature, humidity, pressure, downward longwave radiation, incident short-wave radiation and 10m wind speeds are provided in 3 hour intervals for the model from the North American Regional Reanalysis at a 32.5km resolution (Mesinger et al., 2006). Sea surface albedo is parameterized as a function of solar zenith angle following Briegleb et al. (1986). Solar radiation is attenuated differently as a function of the bathymetry ranging from Jerlov Type 1 (open ocean water) in the basin, to Jerlov Type 7 (dark coastal water) for waters shoreward of the 25m isobath (Paulson & Simpson, 1977).

Freshwater inflow is also supplied to the model from the three largest rivers in the domain, the Yukon, Kuskokwim and Anadyr. Climatological monthly river flow rates are obtained from the USGS (http://waterdata.usgs.gov/) for the Yukon and Kuskokwim and from the NCAR Earth Observation Laboratory Data Center (http://data.eol.ucar.edu/datafile/nph-get/106.ARCSS021/RUSRIVER.txt) for the Anadyr river (following Zhang et al.(2012)). The freshwater volume input of each is specified as distributed point sources along each coastal region representative of their respective deltas. The temperature of the inflow is set to nearby coastal ocean surface water temperature estimated from earlier model runs that did not include riverine input or 0°C, whichever is larger.

2.2 Ice model

As mentioned previously the ice model used in this study originated in a branch version of ROMS as an implementation by P. Budgell (2005). It has been used previously in models of the Bering Sea by Danielson et al. (2011), Danielson et al. (2014), Hermann et al (2013) and Hermann et al. (2016) albeit in a different code version, and likely with different parameters and settings.

The thermodynamics in this model are based on the parameterization of Mellor and Kantha (1989). Ice thickness is represented as a single category within each grid cell with a potential layer of snow and/or meltwater resting above. The equations for the grid-cell averaged thickness of the ice, h_i, and the percent areal coverage of the ice, or ice concentration, c, as implemented in ROMS, are:

$$\frac{Dh_i}{Dt} = \frac{\rho_o}{\rho_i}\left[c\left(w_{io} - w_{ai}\right) + (1-c)w_{ao} + w_{fr}\right] \tag{1}$$

$$\frac{Dc}{Dt} = \frac{\rho_o}{\rho_i}(1-c)\left[\Phi w_{ao} + w_{fr}\right] \tag{2}$$

where the total derivative on the left hand side of the equation includes advection, ρ_o is the seawater density, ρ_i the sea ice density, w_{io} the ice production term at the ice-ocean interface, w_{ai} the negative of the ice production term at the atmosphere-ocean interface, w_{ao} the lateral ice production at the ice edges, w_{fr} the frazil ice production term, and Φ a lateral growth parameter. h_i is the thickness the ice would have if it were spread uniformly over the grid cell. It can vary due to advection, atmosphere-ice heat exchange, ice-ocean heat fluxes, or frazil ice accretion. It is representative of the volume of ice in the cell, rather than the physical ice thickness when c is less than one. Here we label the physical ice thickness $H_I = h_i/c$. Ice concentration c at a given location can change due to advection, atmosphere-ocean heat exchange, or frazil ice formation. It is important to note that Equation 2 is an empirical relationship and the variable φ is a tunable parameter as discussed in the original Mellor and Kantha article (1989). Here we set the value of φ to 3 when w_{ao} is positive, and 0.5 when w_{ao} is negative.

The cell averaged snow and surface melt water thickness are labelled h_{snow} and h_{sfw} respectively. Exchanges at the interface with the atmosphere affect any present snow or meltwater before affecting the ice. Surface meltwater is allowed to reach a maximum of 10 cm thickness (as in Hakkinen and Mellor (1992)). Excess is represented as a low salinity flux to the ocean. The salinity of the meltwater is not tracked in the model but rather is assumed to have a value of 3.2. For the determination of ice conductivity and salt fluxes the salinity of the sea ice is set to $min(S_{surf},3.2)$, where S_{surf} is the surface water salinity. Although this can be a sensitive parameter, it is left unchanged in the modifications discussed below.

In the original ice model implementation, the ice temperature at the interface with the atmosphere is updated with a quasi-implicit scheme that utilizes information about the ice internal temperature from the previous time step along with atmospheric fields and parameterizations for sensible, latent, longwave and shortwave radiation. The longwave radiation is approximated with a Taylor expansion in Mellor and Kantha (1989) such that both the surface temperature from the previous and present time-steps are used. In our implementation, a consistent approximation was provided making use of the downward longwave radiation (Q_{LW}^{dn}) from the atmospheric forcing files, such that the net longwave radiation (Q_{LW}^{net}) at time-step [*n*] is approximated as:

$$Q_{LW}^{net}[n] = \; Q_{LW}^{dn}[n] + 3\varepsilon\sigma(T_s[n-1])^4 - 4\varepsilon\sigma(T_s[n-1])^3 T_s[n], \qquad (3)$$

where ε is the surface emissivity, σ is the Stefan-Boltzmann constant, and T_s is the surface temperature.

The ice model includes a fully explicit implementation of the EVP rheology of Hunke and Dukowicz (1997). The ice momentum equations are

$$\frac{d}{dt}\left(h_i u\right) = h_i f v - h_i g\frac{\partial \zeta_w}{\partial x} + \frac{c}{\rho_i}\left(\tau_a^x + \tau_w^x\right) + \frac{1}{\rho_i}\left(\frac{\partial \sigma_{xx}}{\partial x} + \frac{\partial \sigma_{xy}}{\partial y}\right)$$
$$\frac{d}{dt}\left(h_i v\right) = -h_i f u - h_i g\frac{\partial \zeta_w}{\partial y} + \frac{c}{\rho_i}\left(\tau_a^y + \tau_w^y\right) + \frac{1}{\rho_i}\left(\frac{\partial \sigma_{yx}}{\partial x} + \frac{\partial \sigma_{yy}}{\partial y}\right) \quad (4)$$

where *u* and *v* are components of the ice velocity, *f* is the Coriolis parameter, ζ_w is the sea surface elevation, τ_a is the atmosphere-sea ice drag, τ_w is the ocean-sea ice drag and σ is the internal ice stress tensor. Nonlinear advection terms and curvilinear terms are not considered. A constitutive law describes the relationship between the stress tensor and rates of strain, ε_{ij}, which after adding the elastic term suggested in Hunke and Dukowicz (1997), can be written (using Einstein notation) as,

$$\frac{1}{E}\frac{\partial \sigma_{ij}}{\partial t} + \frac{1}{2\eta}\sigma_{ij} + \frac{\eta - \zeta}{4\eta\zeta}\sigma_{kk}\delta_{ij} + \frac{P}{4\zeta}\delta_{ij} = \varepsilon_{ij} \quad (5)$$

where *E* is Young's modulus, ζ is the bulk viscosity, η the shear viscocity and *P* is a pressure term that is a measure of the ice strength. It is parameterized as linear in h_i and exponential in *c*

$$P = P^* h_i e^{-C_P(1-c)} = 5 \times 10^3\, h_i e^{-20(1-c)} \text{ N m}^{-2} \quad (6)$$

The bulk and shear viscosities, are specified to increase as pressure increases and/or strain rate decreases,

$$\zeta = \frac{P}{2\Delta} \quad (7)$$

$$\eta = \frac{P}{2\Delta e^2} \quad (8)$$

$$\Delta = \left[\left(\varepsilon_{11}^2 + \varepsilon_{22}^2\right)\left(1 + \mu^{-2}\right) + 4\mu^{-2}\varepsilon_{12}^2 + 2\varepsilon_{11}\varepsilon_{22}\left(1 - \mu^{-2}\right)\right]^{1/2} \quad (9)$$

where μ is the ratio of the major to minor axes of the elliptical yield curve, proposed by Hibler (1979) to equal 2

The wind and ocean drag on the ice are both parameterized as functions of ice thickness such that the drag on thinner ice is less. The albedo of the ice/snow/meltwater surface is estimated following Ebert and Curry (1993) with the slight adjustment that if meltwater and ice are present without snow, the albedo is estimated as the average of their estimates for bare ice and meltwater (0.42).

Northern boundary conditions for *c* are obtained by interpolation of satellite radar-derived daily estimates at the northern domain edge grid points. The estimate used for this is from the ARTIST Sea Ice (ASI) Algorithm, using measurements from the Advanced Microwave Scanning Radiometer - Earth Observing System (AMSR-E) for sea ice concentration [Kaleschke et al., 2001; Spreen et al., 2008] from the Integrated Climate Data Center (ICDC, icdc.cen.uni-hamburg.de/), University of Hamburg, Hamburg, Germany. For all other ice-related variables, boundary conditions are established by first running the model with no-gradient conditions at the northern and western boundaries and then using the ice properties obtained at the boundaries from that simulation in a new simulation in which the ice boundary conditions are set to clamped for inflow and no-gradient for outflow. This helps approximate the characteristics of arctic ice entering the domain as no observational data for these variables is available.

This ice model is tightly coupled into ROMS as an internal subroutine such that integration of the sea ice thermodynamic state is a step in the procedure of updating the ocean state. Sea ice related variables are available to the ocean model at the timescale of the baroclinic time step (60s in this case) and vice-versa. The spatial resolution and the c-grid arrangement of the variables in the ice model is identical to that of the ocean model. For the EVP dynamics 60 elastic time steps (1s) are used per viscous time step.

2.3 Modifications to the ice model

The algorithms for the ice model component are described as stated previously in several publications [Budgell, 2005; Hunke & Dukowicz, 1997; Mellor & Kantha, 1989]. But often ambiguities in such natural language descriptions only emerge upon numerical implementation. The foundation for this work was a ROMS implementation provided by Kate Hedstrom in 2014 [Hedstrom, 2014]. At that point the code was under development. In order to achieve satisfactory model performance in our Bering Sea model setup, we had to fix several coding “bugs”, make small numerical adjustments, and introduce physical modifications to the sea ice model component, inspired by a careful reevaluation of the ice model thermodynamics and dynamics. In this section modifications to the ice model implementation are presented. The development cycle, which was repeated numerous times, involved running a simulation of the eastern Bering Sea from initial freeze-up through the spring/summer melt (approximately 9 months), comparing the temporal and spatial patterns of ice concentration with satellite products, and then looking for shortcomings in the implementation that could account for the largest model discrepancies. Over a sequence of simulations, a physical parameterization might be refined, then a bug in the original code is found, then an adjustment to the numerics is deemed necessary. It becomes time-prohibitive to backtrack to do a full sensitivity study to quantify the improvement provided by each modification. So here two simulations are presented that represent the most promising solutions we have obtained to date. Each reproduced the observed ice variability remarkably well, in particular in terms of the area integrated ice concentration. The first of the two simulations , labeled S_{Therm}, includes a set of modifications to the ice thermodynamics (model modifications 1-5 described below), while the second, labeled S_{Dyn}, additionally includes more speculative dynamic adjustments to the drag formulation and ice strength (modifications 6-7 described below).

2.3.1 Thermodynamic adjustments

1. *Adjustments to the surface albedo*. The original model has been augmented to more accurately represent the surface albedo. The effect of albedo on penetrating shortwave radiation can be incorporated into the input forcing files in a typical, ice-free, ROMS implementation, by providing the net shortwave heat flux. However, with the potential for the presence of sea ice, such preprocessing of the downward irradiance presumes the ice albedo to match that of ocean surface water. To allow for both a zenith-angle dependent ocean albedo and a distinct albedo for bare sea ice, snow covered sea ice, or sea ice with snow and/or melt pond coverage, ROMS

forcing files supply the total downward shortwave irradiance at the surface. The seawater albedo is calculated as a function of zenith angle following Briegleb et al. (1986). Albedo for snow, ice, and melt ponds is calculated following an implementation included in the original code that varies albedo as a function of snow and ice thickness but with modification. The original model offered the following parameterization, for bare ice:

$$Alb_{ice} = \begin{cases} 0.082\log\left(\max\left(H_i, 0.01\right)\right) + 0.48 & 0 < H_i < 1 \\ 0.076H_i + 0.41 & 1 \le H_i < 2 \\ 0.56 & H_i \ge 2 \end{cases} \tag{10}$$

and if snow and potentially meltwater overlay the ice,

$$Alb_{snow} = \begin{cases} 0.83 & H_{snow} > 0, H_{sfw} = 0 \\ Alb_{ice} + 10(0.70 - Alb_{ice})H_{snow} & H_{snow} < 0.1, H_{sfw} > 0 \\ 0.70 & H_{snow} \ge 0.1, H_{sfw} > 0 \end{cases} \tag{11}$$

where H_{snow} is the physical snow thickness (h_{snow}/c) and H_{sfw} is the physical melt pool (surface water) thickness (h_{sfw}/c). With this formulation the surface albedo is set to Alb_{snow} whenever snow is present, and set to Alb_{ice} otherwise. But it neglects the case in which there are melt ponds alone over bare sea ice, which the model produced frequently in the Bering Sea in the late spring. Melt ponds generally have a lower albedo than either snow or bare ice but are unlikely to cover the entire ice surface. So as a simple amendment to the parameterization above, the albedo is reduced in the presence of greater than 0.02 m of surface meltwater to a constant value:

$$Alb_{ice/sfw} = \begin{cases} Alb_{ice} & 0 < H_{sfw} < 0.02 \\ 0.42 & H_{sfw} > 0.02 \end{cases} \tag{12}$$

This value is midway between the high-end albedo approximation for melt ponds (0.26) and the low-end estimate for bare ice (0.58) provided in Ebert and Curry (1993).

2. *Inclusion of the latent heat fluxes associated with precipitation.* The NARR atmospheric model used here includes information on the phase of precipitation, distinguishing four classes (rain, freezing rain, snow and ice pellets). Snow and ice pellet categories are considered frozen precipitation that melt on contact with the sea surface or on ice if melt ponds are present. Rain and freezing rain are assumed to freeze when contacting snow or bare ice. In each case the latent heat flux associated with the phase transformation is added. As an example of the magnitude of this latent heat contribution, in order for sea ice to freeze rain falling at a rate of 0.01m day^{-1}, the ice draws away approximately 39 W m^{-2} of heat from the falling water. The sensible heat contribution of the precipitation is already considered in the model using the aforementioned bulk flux algorithm (Fairall et al., 2003) which assumes that the precipitation temperature is related to the air temperature. We assumed that this formulation remains reasonably valid for solid phase precipitation. At times, rain or frozen rain can fall at surface air temperatures below freezing or snow can fall when the near-surface air temperatures is above freezing. The early versions of this model determined the phase of the precipitation based on the air temperature. In the simulations presented here, the phase is used as predicted by the atmospheric model and correction to the atmosphere-ice or atmosphere-ocean heat flux is made, to account for the phase transitions.
3. *Improved representations of snow and melt pond evolution*. In the original formulation, as the ice concentration in a grid cell decreased, the associated melt pond and/or snow volume did not change. In our modification, h_{snow} and/or h_{sfw} diminish proportionally as the fractional area (*c*) of ice coverage decreases due to thermodynamic processes. The associated low-salinity or fresh water (in the case of snow) flux is added to the ocean. As *c* increases due to thermodynamic processes in the absence of precipitation, the pre-existing volume of snow or melt water is assumed to remain unchanged. Consequently, H_{snow} and/or H_{sfw} are reduced (h_{snow} and h_{sfw} are

held constant). In these simulations, a maximum limit of 0.1 meters was set for h_{sfw}, but as the ice becomes thinner than this, this maximum limit is reduced such that h_{sfw} is always less than or equal to h_i. The excess meltwater contributes a low salinity flux to ocean.

4. *An expanded decision tree for determining ice surface state.* As we mentioned previously, the surface of the ice-covered portion of each model grid cell could be bare ice, snow, snow with melt ponds, or bare ice with melt ponds. Whether freezing or melting occurs at this surface depends on the net heat flux to the ice surface (Q_{surf}), the ice surface temperature (T_{is}) and the phase (ice, snow and/or meltwater) that is present at the interface. When T_{is} is at the freezing point and the heat flux is into the ice, ice/snow should melt to produce meltwater. But situations also arise where the estimated ice surface temperature is at the freezing point but the heat flux is out of the ice, and meltwater would freeze and thus increase h_i, whereas in the absence of meltwater the only effect would be to cool the ice or snow. The determination of the effect of the surface flux on h_i, h_{snow}, and h_{sfw} depends on the presence or absence of snow, the presence or absence of meltwater, the estimated surface temperature and the sign of the surface flux. Each of these dependencies is binary except for T_{is} in which case it is sometimes necessary to distinguish temperatures above the freezing point of sea ice (T_{frz}=-0.17°C) from those that reach the freezing point of snow (0°C) . To properly account for all combinations of possible results, a decision tree is implemented in the modified model as shown in Figure 3. Green leaf nodes indicate cases which were handled correctly in the ROMS implementation we started with, red leaf nodes indicate cases that either were handled wrong or were not considered. As one example, freezing of meltwater would not occur in the original model when $T_{is} < T_{frz}$, Q_{surf} is negative, and no snow is present. In our version, there are a number of cases where ice, snow and meltwater layer thickness do not change because Q_{surf} at the estimated surface temperature would act to cool or warm the phase present at the surface towards freezing point rather than

melt or freeze ice directly. Despite the potential for the snow melting, in all cases, the meltwater ponds are considered to have a salinity of 3.2 (as specified in the original formulation), as if produced by the melting of sea ice since meltwater salinity is not tracked in the model.

5. *Numerical bounds on the internal ice temperature*. The Mellor and Kantha thermodynamics (1989) evolve the internal ice temperature, T_i, based on the ice (and potentially snow) thickness along with estimates of the ice surface temperature, T_{is} , and the molecular sublayer temperature at the ice-ocean interface, T_o. In simulations using the earlier code it was found that the estimate of internal temperature could unreasonably exceed both T_{is} and T_o for extended periods of time or that it could remain fixed at the freezing point of freshwater (the model initial value) well into the winter season despite significant ice growth. These errors were deemed to be numerical in nature and a simple fix of limiting T_i to fall between T_{is} and T_o and never exceed T_{frz} allowed T_I to evolve in a realistic manner.

2.3.2 Dynamics adjustments

6. *Ice-ocean, and air-ice drag coefficients*. In model tests that included all of the modifications above, comparison with satellite estimates of spatial distribution of ice concentration still showed poor agreement in response to wind events throughout the winter season, particularly in island polynyas, at the ice edge, and along the Alaskan coast. For example, where satellite imagery showed sea ice becoming separated from the western coast of Alaska under the influence of easterly winds, the model showed mostly stationary nearshore sea ice. Farther offshore the model response was more consistent with the ice movement implied by the satellite imagery. The ice-ocean quadratic drag formulation in the model calculates the drag coefficient C_D^{iw} at time step *n* as

$$C_D^{iw}\left[n\right] = \frac{\kappa u_{iw}^{*}}{\log\left(\max\left(\frac{z}{z_o}, a_1\right)\right)} \tag{13}$$

where κ=0.4,

$$u_{iw}^{*} = max\left[\left\{C_D^{iw}[n-1]\left((u_w - u_i)^2 + (v_w - v_i)^2\right)\right\}^{\frac{1}{2}}, 0.0001\ m/s\right] \tag{14}$$

z is the top model layer thickness and $z_o = min(max(a_2 H_i, 0.01\ m), 0.1\ m)$. In the default parameterization a_1 =3 and a_2 = 0.02. Visual comparison of the movement of sea ice in the model with satellite microwave estimates (by comparison of sequences of daily snapshots) suggested that in shallow coastal regions with thick ice, the value of C_D^{iw} was too large. This unrealistically limited the sea ice movement in response to wind events. In order to decrease the excessive drag in the thick ice along the Alaskan west coast, we set a_1 = 6 and a_2 = 0.01. With this modification the model performance improved along the Alaskan west coast, however the island polynya regions (St. Lawrence, and St. Matthew) still exhibited higher ice concentrations in response to wind events than was observed in the satellite imagery.

The default setting for the atmosphere-ice drag coefficient varied depending on the choice of bulk flux (atmosphere-ocean exchange) algorithm in the ROMS model. For the option of using the Fairall et al. formulation (2003) that is packaged with the standard ROMS, C_D^{ai} is specified as spatially uniform and constant ($C_D^{ai} = 0.003$ by default). In order to allow the wind-ice drag to increase as a function of ice thickness, the coupled model was modified to calculate this drag as

$$C_D^{ai} = 0.003\left[1 - \cos\left(\pi \min\left(H_i + 0.05, 1.0\right)\right)\right] \tag{15}$$

This is consistent, but with different coefficient values, to the implementation of the ice-ocean drag coefficient in the Fairall algorithm in the Bergen Climate Model (Furevik et al., 2003).

7. *Ice Strength*, P^*. The effect of modification 6 was to allow thicker ice to be transported more effectively by wind stress and less effectively by ocean currents. While this alone improved ice concentration distributions, the gradient of ice concentration at the ice edge remained much lower than in satellite estimates, and at times appeared exacerbated by the increased wind-transport of thicker ice. This was notably improved by adjusting parameters in the ice strength formulation. Ice strength is calculated using the formulation in Eq. 4 where parameter P^* is increased from $5\text{x}10^3$ N m^{-2} in the original formulation to $25\text{x}10^3$ N m^{-2} and C_P from 20 to 27. These adjustments are consistent with the usage in a similar model by Olason and Harms (2010) when modeling polynyas. The primary impact is to make the ice strength higher at high ice concentration. Simulations were also performed using a quadratic ice strength (Overland & Pease, 1988) but these are not discussed here because they failed to reproduce observations of sea ice concentration well.

An example of the improvement to the ice concentration distribution along the northern Bering Sea coastlines due to dynamical modifications 6 and 7 is presented in Figure 4. In response to sustained southward winds prior to this date, open water areas develop along the Chukotka, Seward and St. Lawrence island coastlines, e.g., as is seen in the ASI imagery (Fig. 4, bottom). The S_{Dyn} simulation captures this but S_{Therm} does not. Additional time-series comparisons of the integrated c in the polynya area south of St. Lawrence island will be shown below. Note that the combined effect of the two modifications to the drag at the top and bottom of the ice layer increase the sea ice response to wind stress relative to ocean current stress. The open water area that is visible between the Chukotka peninsula and St. Lawrence Island in S_{Therm} likely results from the ice being advected too strongly with the northeastward flowing Anadyr current. This feature is not found in the ASI image or S_{Dyn}.

3 Model-observation comparison

Ice concentration is the most accessible variable for comparisons between the model and observations. The simulation results are compared with two satellite products to assess performance. One is a component of the Operational Sea Surface Temperature and Sea Ice Analysis (OSTIA) (Donlon et al., 2012) product. It offers daily composite ice concentration estimates at approximately 12.5 km resolution, using data from several Special Sensor Microwave Imager (SSM/I) satellites, processed for EUMETSAT (Andersen et al., 2007). The second is a higher resolution product based on the Arctic Radiation and Turbulence Interaction STudy Sea Ice algorithm (ASI) (Spreen et al., 2008), that uses the higher frequency channel of the Advanced Microwave Scanning Radiometer. This product obtains ice concentration estimates at approximately 5 km resolution. Each product has shortcomings. OSTIA often over-smooths the concentration fields failing to resolve polynyas or the sharp gradients which develop at the ice edge with on-ice winds. ASI represents polynyas better but can exhibit rapid fluctuations in ice concentration due to signal interference from clouds. Based on visual comparisons for each day in the winter of 2009-10, both products exhibited an ice edge in the Bering Sea (indicated by the 1% ice concentration contour) that, in general, is very similar to the ice edge estimate from the Multisensor Analyzed Sea Ice Extent produced by the United States National Ice Center/National Snow and Ice Data Center (National Ice Center (NIC) And NSIDC, 2010).

The model prediction of sea ice advance and retreat can be quantified by calculating the fraction of the Bering Sea shelf covered in ice as a function of time:

$$F_i = \frac{1}{A_s} \sum_{j=1}^{N_s} c_j(t) \Delta x \Delta y \tag{16}$$

where A_s is the shelf area between the coast and the 200m isobath as measured in the model, the sum is over the N_s grid cells on the shelf, c_j refers to the ice concentration in the j-th grid cell and $\Delta x \Delta y$ is the surface area of the grid cell. For the purpose of this calculation and those that follow, both the OSTIA and ASI satellite estimate are interpolated onto the model grid (2 km x 2 km).

The two model solutions, S_{Therm} and S_{Dyn}, compare well with the satellite estimates after implementing the modifications outlined in section 2 (Figure 5a), capturing the timing of ice advance, peak areal coverage and ice retreat. The result from one of our original simulations with the unmodified ice model is also shown in Figure 5a (dashed line). It exhibited a late onset of freezing, a diminished seasonal maximum in F_i, and delayed melting.

The improved model results also capture the weather scale variability, showing a decrease in F_i for each event in which the wind shifts to having a northward component (red arrows in *Figure 5*b) and warming air temperature (*Figure 5*c). Coherence between F_i and the modeled northward wind component (using Welch's method) are greater than 0.7 for both experiments for frequencies associated with 7 to 14 day variability, with the values for S_{Dyn} slightly higher than for S_{Therm}. However often the magnitude of the weather-related modulation in F_i is less in the model than the satellite estimates. The ASI estimate in particular can exhibit changes in F_i as large as -10% presumably in response to brief wind reversals (as in late-December 2009). But as mentioned previously this satellite estimate is susceptible to interference from clouds which may also be correlated with such weather events. The differences between the simulations indicate the effect of the adjustments to the ice dynamics. Having a thickness dependent air-ice drag helps reproduce the seasonal peak areal coverage in mid-March, but at the cost of a slightly early ice retreat in April and May. The model underestimates the initial ice advance from mid-November to early December. Careful comparison of sequences of the ASI and model ice concentration fields suggests that this underestimate results primarily from a weaker ice inflow through the Bering Strait from the Arctic and is also affected by slower ice formation in Norton Sound. The ice inflow from the Chukchi to the Bering Sea can possibly be improved with a better choice of the ice boundary conditions in the north. Examining sequences of maps during the ice retreat period shows that the early melt occurs primarily in the region of the Anadyr current south of the Chukotka peninsula, similarly in the model and observations.

Another metric for comparing the model with the satellite observations is the average ice concentration per grid cell (Figure 6 a):

$$\overline{c_S} = \frac{1}{N_S^i(t)} \sum_{k=1}^{N_S^i(t)} c_k(t) \tag{17}$$

where N_S^i is the number of grid cells on the Bering Sea shelf that have greater than 0.1% ice coverage and *k* is an index that runs over those cells. This is a measure of how densely packed the sea ice is. Over the course of the winter the average concentration per cell increases rapidly in November, then much more gradually between December and late March, before beginning to decrease in the spring. The two improved model solutions generally fall between the ASI and OSTIA estimates of $\overline{c_S}$. ASI tends to exhibit the most compact arrangement of the ice, while not surprisingly the OSTIA estimate, being lower resolution, estimates the lowest average concentration per grid cell.

Ice extent is defined here as the fraction of the shelf grid cells containing greater than 0.1% ice coverage (Figure 6b):

$$F_{ext} = \frac{N_S^i(t)}{N_S}. \tag{18}$$

Both improved simulations produce larger than observed F_{ext} between December 2009 and March 2010, but fall roughly between those estimates later in the season.

Despite similar characteristics throughout most of the season, the two model simulations differ noticeably in terms of the thickness of the ice produced and hence the total volume (*Figure 6*c). At the seasonal peak the average value of H_i is approximately 0.4 m thicker in S_{Therm} than in S_{Dyn} and the total ice volume is about 25% greater. Sea ice that is thicker than 0.45m is more effectively accelerated by wind forcing in the S_{Dyn} simulation (while ice thinner than this threshold is less effectively transported). This leads to thick ice being transported southward with the predominant winter winds more in S_{Dyn} . F_{ext} is larger in S_{Dyn} because the ice spreads over a larger number of shelf grid cells (see *Figure 5*b). In the same simulation, h_i is smaller on average because the thick ice is transported away from the strong generation regions more rapidly. The shelf average ocean temperature at the end of March is approximately 0.2 degrees warmer in S_{Dyn} than S_{Therm}. This suggests that the higher F_i in S_{Dyn} reduces the loss of heat to the atmosphere which may further inhibit thick ice growth.

Over the course of the winter season the distribution of ice concentration varies. Based on satellites, sea ice is more likely to be found at lower concentration early and late in the season (*Figure 7*), and not surprisingly at higher concentration in the months of maximum ice extent. Based on the ASI and two model estimates a majority of the 2km x 2km shelf grid cells that contain ice in February and March have *c* over 90%. The lower resolution OSTIA product places highest probability in the 80 to 90% range. The models tend to place a higher likelihood of grid cells with very low concentration of ice early in the season compared to the satellite estimates, but this may be more a result of inaccuracy of the satellite measurements at low concentrations (Meier et al., 2015) rather than model error.

Very little of the sea ice in the Bering Sea is landfast. Floe trajectories estimated from satellite imagery suggest that sea ice may drift tens of kilometers a day in response to winds and currents (Sullivan et al., 2014). This at times causes the exposure of wide bands of open water along the various coastlines. As a method for quantifying the overall ice position and movement along with the general southward expansion of the sea ice, a two-dimensional ‘center of mass’ is calculated with ice concentration taking on the role of “density”(Figure 8). Ice thickness is neglected here, to make direct comparison with the satellite estimates of *c*. The center-of-mass coordinates are calculated as:

$$\varphi_{COM}(t) = \frac{1}{N_S^i(t)} \sum_{k=1}^{N_S^i(t)} c_k(t)\varphi_k \tag{19}$$

$$\theta_{COM}(t) = \frac{1}{N_S^i(t)} \sum_{k=1}^{N_S^i(t)} c_k(t)\theta_k \tag{20}$$

Where φ_{COM} and $\theta_{COM}(t)$ indicate the longitude and latitude of the center of mass and φ_k and θ_k indicate the longitude and latitude of a grid cell which contains greater than 0.1% ice coverage. The velocity of the center-of-mass can then be approximated by calculating the geodesic distance between sequential daily center-of-mass positions (Figure 8c).

In the winter of 2009-2010, θ_{COM} advanced southward at a rate as high as 1.5° per month (in January 2010) reaching its southernmost latitude by mid-March. S_{Therm} more closely matches with the satellite estimates of this position, as S_{Dyn} tends to place the center-of-mass farther southward. Conversely, S_{Dyn} more closely matches the fluctuations in φ_{COM} over the course of the season as compared to the satellite estimates (ASI in particular). This difference can be related to the mechanisms that are likely causing the fluctuations in the two directions. The latitudinal position of the center-of-mass depends more on the total area of ice produced, pushing southward as more sea ice is produced in the northern portion of the domain. The east-west movement of the ice center-of-mass is more directly related to the wind forcing. The S_{Dyn} experiment tends to overestimate the ice area (*Figure 5*a), but allows the sea ice to be more responsive to wind drag. Comparison of the center-of-mass velocity vectors in Figure 8c shows that the direction of movement of the center of mass for both simulations correlate well with the satellite product estimates, but both tend to underestimate the magnitude . S_{Dyn} in general does better though with an average center-of-mass speed for December 2009 through April 2010 of 6.7 km day^{-1} compared to 3.8 km day^{-1} for S_{Therm} where the ASI and OSTIA estimates are 10.5 and 8.6 km day^{-1} respectively.

The better response of S_{Dyn} with respect to ice movement is also apparent in polynya regions. A comparison of the open-water area in the polynya region south of St. Lawrence Island as a function of time is displayed in Figure 9. Here the open water area, O_w, is displayed as a fraction of the total surface water area in the region delineated in Figure 1,

$$O_w = \frac{1}{A_{slb}} \sum_{j=1}^{N_{slb}} (1 - c_j(t)) \Delta x \Delta y \qquad (21)$$

where A_{slb} is the total area of coastal ocean within the box and the sum is over the total number of oceanic grid cells (N_{slb} in the box). Over the winter season, as winds shift direction, the polynya experiences multiple openings and closings. This appears to be best captured by the ASI satellite product which shows ice repeatedly vacating and filling the coastal region south of St. Lawrence Island. The lower resolution and higher level of temporal and spatial smoothing of OSTIA produces very little variability. S_{Therm}, which shows significant improvement compared to S_{Orig} based on other metrics, does a worse job of estimating the overall ice cover in this polynya region. Both S_{Therm} and S_{Orig} also exhibit less extreme fluctuations in open water area on the weather-event time scale than is suggested by ASI. S_{Dyn},while still not exhibiting quite the magnitude of fluctuations in O_w that ASI does, replicates the overall pattern of repeated polynya development and disappearance rather well. As will be presented in more detail in Part 2, although O_w for S_{Dyn} and S_{Orig} look rather similar in Figure 9, S_{Dyn} does a significantly better job of reproducing the distribution of ice among the grid cells within this region. For example during a period of strong polynya-favorable winds (January 28th-February 7th 2010), it produced completely ice-free grid cells along the southern coast of St. Lawrence Island, where S_{Orig} produced a larger area of partially covered grid cells.

The spatial distribution of seasonally averaged ice concentration is calculated from the ASI observations over the period with significant sea ice coverage (November 15th, 2009 – May 31st, 2010) (*Figure 10*a).

The highest averaged ice concentrations are found along the eastward facing portion of the Chukotka coast, the westward facing portion of the Alaska coast and in the Bering Strait region. The S_{Dyn} simulation (Figure 10b) does well in capturing these regions of highest concentration, albeit with slightly lower peak average concentrations. The S_{Dyn} simulation also captures the reduced ice concentration in polynya regions along the southward-facing Chukotka Peninsula coast, the westward-facing Seward Peninsula coast and on the south sides of both St. Lawrence and St. Matthew islands. The S_{Dyn} simulation overestimates ice concentration (relative to ASI) in the shallowest portion of Norton Sound, in the region of the Koyuk river estuary (Northeast corner of Norton Sound, 161.2°W and 64.9°N). It is possible that riverine outflow from this source (particularly late in the season), which is neglected in the model, transports sea ice away from this region. S_{dyn} also exhibits higher ice concentrations than ASI in the vicinity of the shelf break (between the 100m and 150m isobaths) (Figure 10c). This is likely the result of adjustment to the wind drag formulation, causing ice to be transported more strongly in the direction of the prevailing winds. Adjusting the parameters of the wind drag formulation to attain better agreement at the ice edge is of course an option, however, comparison in the polynya regions argues for an adjustment in the opposite direction, as concentrations remain too high in the model in these regions. As was expected, the standard deviation in the ice concentration (Figure 10d) tends to be highest on the outer Bering Sea shelf where ice is only found at the peak of the winter season, and is lowest in regions that have the highest average seasonal concentration. The spatial distribution of the standard deviation in *c* for S_{Dyn} matches well with the satellite estimate over much of the shelf (Figure 10e) and it shows mismatches in most of the same locations where the seasonal average concentration estimate is off (Figure 10f).

Similar analyses were done for solution S_{Therm} and the difference plots are shown in Figure 11. In S_{Therm}, the seasonal average ice concentration not only has too little ice on the outer shelf, but also far too much ice on average along the coasts where polynyas frequently develop (Figure 11a). The S_{Therm}

simulation underestimates the ice concentration variance in general (Figure 11b). This is likely due to the more limited movement of the ice in response to winds in this simulation.

The model-observation comparisons presented above do not single out either the S_{Dyn} or the S_{Therm} as being clearly favorable. By some measures, such as the fractional ice coverage in Figure 5a, S_{Therm} matches more closely with the satellite estimates, but by other measures, such as the mean and variance of the spatial distribution (Figure 10 and Figure 11), S_{Dyn} may be judged preferable. Certainly further exploration of parameter space may yield a compromise between the two that is superior to both. Alternately, improvement of some other portion of the parameterized ice physics might produce a substantial improvement. However the performance in these two simulations is encouraging in how much of the weather-scale to seasonal variability in the sea ice is being captured.

For the last of the model-data comparisons (Figure 12), results from S_{Dyn} are utilized (although these are mostly consistent with the S_{Therm} solution). Here, the daily average spatial maps of sea ice concentration and sea surface temperature (SST) are presented for 5 selected days over the course of the winter season. The OSTIA and ASI products are shown alongside the model estimates (in the middle column). Note the ASI does not come with its own SST estimate. In general, there is good agreement between the model and observations with a few exceptions. As mentioned above, at the start of the winter season, ice formation in the model lags the satellite estimates particularly in Norton Sound (Figure 12 a, b, c). In general, during this period, modeled temperatures on the Bering Sea shelf are 1-2^{o}C higher than satellite estimates. Similarly, comparison with the OSTIA estimate suggests that the modeled surface waters warm too quickly in the spring (Figure 12 m, n, o), which may contribute to the premature ice melt in the model. The OSTIA SST estimation in regions partially covered by sea ice is a relaxation to climatology or the freezing temperature of sea water depending on ice concentration (Donlon et al., 2012) and therefore may be inaccurate on the Bering Sea shelf over much of the winter season. Nonetheless the discrepancy between model and satellite estimate extends into the Bering Sea Basin.

Another region where the model exhibits differences from the satellites is at the seaward ice edge. At times during the ice advance, the modeled ice distribution exhibits strong meanders and filamentous structures on the mid-to-outer Bering Sea shelf (Figure 12e). As these features develop, they coincide with comparable patterns in the shelf salinity, suggesting that they result from the coupling between the ice and ocean surface currents. The fact that similar patterns are not found, even in the higher resolution satellite imagery, suggests that either the applicability of the ice rheology at these reolutions is limiting or that the model does not have enough resolution to allow small-scale eddy variability along the ice edge frontal region that could potentially change the frontal dynamics and smear out these strong corrugations in the ice edge geometry. It remains to be shown, using models of higher resolution, whether these large scale ice edge corrugations can be dispersed by submesoscale processes (Capet et al., 2008) that our model does not resolve.

4 Summary

This study documents efforts to improve the performance of a single-category sea ice model in the Eastern Bering Sea. Extensive critical evaluation of the algorithm and experimentation with refinements to the ice thermodynamics and dynamics resulted in a set of modifications that exhibited much improved sea ice concentrations for the winter of 2009-10. This suggests that this relatively computationally economical class of models can produce accurate representations of sea ice in the Bering Sea in other winters as well, and is likely applicable to other marginal seas where the sea ice is only seasonal.

The thermodynamic modifications amounted to a more accurate accounting of the surface heat fluxes than was previously incorporated into the scheme. These adjustments led to the model more accurately estimating the timing of freeze-up and melt in the Bering Sea, as well as the areal ice coverage over the full seasonal cycle. The dynamic modifications primarily were to increase the wind drag on the ice as a function of ice thickness, and reduce the ocean drag on the ice (relative to the original formulation) in regions of thick ice along the Alaskan coast. These adjustments led to better representation of the opening and closing of polynyas and an improved gradient in ice concentration at the outer-shelf ice edge.

Satellite-derived ice concentration is the primary observational dataset available for evaluation of the modeled sea ice. Despite this data being limited in spatial resolution and subject to a variety of uncertainties associated with the processing of the reflected microwave signal, it can provide a wealth of information beyond simple comparison of instantaneous ice concentration maps. In this study, we define a set of metrics using these datasets to evaluate the relative performance of the different ice model modifications. These metrics provide information about the overall ice areal coverage, the ice distribution, the seasonal evolution of the ice coverage and the ice movement in response to atmospheric forcing at the weather event scale. Application of this set of metrics not only allowed for evaluation of the ice model, but also provided a means to discern aspects of the ice model formulation that required further refinement.

The modifications described here do not represent an endpoint in the development of this model parameterization, but rather indicate two steps forward in the process of improving the representation it produces. Further improvements may come as more observational information is gathered on the winter vertical structure under the ice and the ice thickness distribution. Further model verification will be accomplished by evaluating other winter seasons and by applying this model setup to other marginal sea areas with seasonal ice. We think that successful implementation of more complex models, such as multicategory EVP types or discrete element method models, will require the same level of attention to the treatment of interaction between all the fluid phases at the atmosphere-ocean interface.

Additionally, it cannot be ignored that any ice-ocean model that is not fully coupled with an atmospheric model can be biased by the forcing that the atmospheric model provides. The atmospheric model has been run with the sea surface state specification that presupposes a sea ice concentration, which in turn affects atmospheric temperature, humidity and winds, all of which are input to the ocean model. An atmospheric model such as NARR, with a 32 km horizontal resolution, will undoubtedly under-resolve variability along coastlines and may cause inaccuracies in the representation of polynya regions. Higher resolution atmospheric model forcing from recently available products such as the 15 km resolution Arctic System Reanalysis ("Arctic System Reanalysis version 2," 2017) may improve the performance of this model in polynya regions, or it may lead to the necessity of re-tuning model parameters. Under-resolving the open water areas of polynyas likely leads to underestimates of air temperature and humidity along with inaccurate surface wind patterns in proximity to these regions. Further model development will benefit from consideration of the sensitivity to the choice of atmospheric forcing.

Acknowledgements: This research was partially supported by the the NASA grant NNX13AD89G. Satellite data was obtained from the OSTIA data repository (http://ghrsst-pp.metoffice.com/pages/latest_analysis/ostia.html) and the ASI data repository (https://seaice.uni-bremen.de/start/data-archive/). Many thanks to Dr. Kate Hedstrom for useful conversations and for providing us with the ROMS core sea ice model code.

5 Bibliography

Andersen, S., Breivik, L. A., Eastwood, S., Godoy, O., Lind, M., Porcires, M., & Schyberg, H. (2007). *Ocean & sea ice SAF sea ice product manual version 3.5*. Retrieved from http://saf.met.no/docs/ss2_pmseaice_v3p5.pdf

Arctic System Reanalysis version 2. (2017). Research Data Archive at the National Center for Atmospheric Research, Computational and Information Systems Laboratory. https://doi.org/10.5065/D6X9291B

Armitage, T. W. K., Bacon, S., Ridout, A. L., Thomas, S. F., Aksenov, Y., & Wingham, D. J. (2016). Arctic sea surface height variability and change from satellite radar altimetry and GRACE, 2003–2014. *Journal of Geophysical Research: Oceans*, *121*(6), 4303–4322. https://doi.org/10.1002/2015JC011579

Briegleb, B. P., Minnis, P., Ramanathan, V., & Harrison, E. (1986). Comparison of Regional Clear-Sky Albedos Inferred from Satellite Observations and Model Computations. *Journal of Climate and Applied Meteorology*, *25*(2), 214–226. https://doi.org/10.1175/1520-0450(1986)025<0214:CORCSA>2.0.CO;2

Budgell, W. P. (2005). Numerical simulation of ice-ocean variability in the Barents Sea region. *Ocean Dynamics*, *55*(3–4), 370–387. https://doi.org/10.1007/s10236-005-0008-3

Capet, X., McWilliams, J. C., Molemaker, M. J., & Shchepetkin, A. F. (2008). Mesoscale to Submesoscale Transition in the California Current System. Part I: Flow Structure, Eddy Flux, and Observational Tests. *Journal of Physical Oceanography*, *38*(1), 29–43. https://doi.org/10.1175/2007JPO3671.1

Chassignet, E. P., Hurlburt, H. E., Smedstad, O. M., Halliwell, G. R., Hogan, P. J., Wallcraft, A. J., et al. (2007). The HYCOM (HYbrid Coordinate Ocean Model) data assimilative system. *Journal of Marine Systems*, *65*(1–4), 60–83. https://doi.org/10.1016/j.jmarsys.2005.09.016

Cheng, W., Curchitser, E., Ladd, C., Stabeno, P., & Wang, M. (2014). Influences of sea ice on the Eastern Bering Sea: NCAR CESM simulations and comparison with observations.

Deep Sea Research Part II: Topical Studies in Oceanography, *109*, 27–38. https://doi.org/10.1016/j.dsr2.2014.03.002

Clement, J. L., Maslowski, W., Cooper, L. W., Grebmeier, J. M., & Walczowski, W. (2005). Ocean circulation and exchanges through the northern Bering Sea—1979–2001 model results. *Deep Sea Research Part II: Topical Studies in Oceanography*, *52*(24), 3509–3540. https://doi.org/10.1016/j.dsr2.2005.09.010

Clement Kinney, J., Maslowski, W., & Okkonen, S. (2009). On the processes controlling shelf–basin exchange and outer shelf dynamics in the Bering Sea. *Deep Sea Research Part II: Topical Studies in Oceanography*, *56*(17), 1351–1362. https://doi.org/10.1016/j.dsr2.2008.10.023

Danielson, S., Weingartner, T., Aagaard, K., Zhang, J., & Woodgate, R. (2012). Circulation on the central Bering Sea shelf, July 2008 to July 2010. *Journal of Geophysical Research: Oceans*, *117*(C10), n/a-n/a. https://doi.org/10.1029/2012JC008303

Danielson, S. L., Weingartner, T. J., Hedstrom, K. S., Aagaard, K., Woodgate, R., Curchitser, E., & Stabeno, P. J. (2014). Coupled wind-forced controls of the Bering–Chukchi shelf circulation and the Bering Strait throughflow: Ekman transport, continental shelf waves, and variations of the Pacific–Arctic sea surface height gradient. *Progress in Oceanography*, *125*, 40–61. https://doi.org/10.1016/j.pocean.2014.04.006

Danielson, Seth, Curchitser, E., Hedstrom, K., Weingartner, T., & Stabeno, P. (2011). On ocean and sea ice modes of variability in the Bering Sea. *Journal of Geophysical Research*, *116*(C12). https://doi.org/10.1029/2011JC007389

Donlon, C. J., Martin, M., Stark, J., Roberts-Jones, J., Fiedler, E., & Wimmer, W. (2012). The Operational Sea Surface Temperature and Sea Ice Analysis (OSTIA) system. *Remote Sensing of Environment*, *116*, 140–158. https://doi.org/10.1016/j.rse.2010.10.017

Durski, S. M., Kurapov, A., Zhang, J., & Panteleev, G. . (2016). Circulation in the Eastern Bering Sea: Inferences from a 2-km-resolution model. *Deep Sea Research Part II: Topical Studies in Oceanography*, *134*, 48–64. https://doi.org/10.1016/j.dsr2.2015.02.002

Ebert, E. E., & Curry, J. A. (1993). An intermediate one-dimensional thermodynamic sea ice model for investigating ice-atmosphere interactions. *Journal of Geophysical Research: Oceans*, *98*(C6), 10085–10109. https://doi.org/10.1029/93JC00656

Fairall, C. W., Bradley, E. F., Hare, J. E., Grachev, A. A., & Edson, J. B. (2003). Bulk Parameterization of Air–Sea Fluxes: Updates and Verification for the COARE Algorithm. *Journal of Climate*, *16*(4), 571–591. https://doi.org/10.1175/1520-0442(2003)016<0571:BPOASF>2.0.CO;2

Flather, R. A. (1976). *A tidal model of the northwest European continental shelf.* (Memoires de la Societe Royale des Sciences de Liege 6 No. 10) (pp. 141–164).

Furevik, T., Bentsen, M., Drange, H., Kindem, I. K. T., Kvamstø, N. G., & Sorteberg, A. (2003). Description and evaluation of the bergen climate model: ARPEGE coupled with MICOM. *Climate Dynamics*, *21*(1), 27–51. https://doi.org/10.1007/s00382-003-0317-5

Häkkinen, S., & Mellor, G. L. (1992). Modeling the seasonal variability of a coupled Arctic ice-ocean system. *Journal of Geophysical Research: Oceans*, *97*(C12), 20285–20304. https://doi.org/10.1029/92JC02037

Hedstrom, K. (2014). *Regional Ocean Modeling System (with Ice)*. Retrieved from https://github.com/kshedstrom/roms

Hermann, A. J., Gibson, G. A., Bond, N. A., Curchitser, E. N., Hedstrom, K., Cheng, W., et al. (2013). A multivariate analysis of observed and modeled biophysical variability on the Bering Sea shelf: Multidecadal hindcasts (1970–2009) and forecasts (2010–2040). *Deep Sea Research Part II: Topical Studies in Oceanography*, *94*, 121–139. https://doi.org/10.1016/j.dsr2.2013.04.007

Hermann, A. J., Gibson, G. A., Bond, N. A., Curchitser, E. N., Hedstrom, K., Cheng, W., et al. (2016). Projected future biophysical states of the Bering Sea. *Deep Sea Research Part II: Topical Studies in Oceanography*, *134*, 30–47. https://doi.org/10.1016/j.dsr2.2015.11.001

Hibler, W. D. (1979). A Dynamic Thermodynamic Sea Ice Model. *Journal of Physical Oceanography*, *9*(4), 815–846. https://doi.org/10.1175/1520-0485(1979)009<0815:ADTSIM>2.0.CO;2

Hu, H., & Wang, J. (2010). Modeling effects of tidal and wave mixing on circulation and thermohaline structures in the Bering Sea: Process studies. *Journal of Geophysical Research: Oceans*, *115*(C1), C01006. https://doi.org/10.1029/2008JC005175

Hunke, E. C., & Dukowicz, J. K. (1997). An Elastic–Viscous–Plastic Model for Sea Ice Dynamics. *Journal of Physical Oceanography*, *27*(9), 1849–1867. https://doi.org/10.1175/1520-0485(1997)027<1849:AEVPMF>2.0.CO;2

Hunke, Elizabeth C. (2001). Viscous–Plastic Sea Ice Dynamics with the EVP Model: Linearization Issues. *Journal of Computational Physics*, *170*(1), 18–38. https://doi.org/10.1006/jcph.2001.6710

Kaleschke, L., Lüpkes, C., Vihma, T., Haarpaintner, J., Bochert, A., Hartmann, J., & Heygster, G. (2001). SSM/I Sea Ice Remote Sensing for Mesoscale Ocean-Atmosphere Interaction

Analysis. *Canadian Journal of Remote Sensing*, *27*(5), 526–537. https://doi.org/10.1080/07038992.2001.10854892

Ladd, C., & Stabeno, P. J. (2012). Stratification on the Eastern Bering Sea shelf revisited. *Deep Sea Research Part II: Topical Studies in Oceanography*, *65*(Supplement C), 72–83. https://doi.org/10.1016/j.dsr2.2012.02.009

Mauch, M., Durski, S. M., & Kurapov, A. (2019). Connectivity of the Aleutian North Slope Current and Bering Sea basin waters at the level of the subsurface temperature maximum: a modeling study. *Journal of Geophysical Research: Oceans*, *In Press*.

Meier, W. N., Fetterer, F., Stewart, J. S., & Helfrich, S. (2015). How do sea-ice concentrations from operational data compare with passive microwave estimates? Implications for improved model evaluations and forecasting. *Annals of Glaciology*, *56*(69), 332–340. https://doi.org/10.3189/2015AoG69A694

Mellor, G. L., & Kantha, L. (1989). An ice-ocean coupled model. *Journal of Geophysical Research: Oceans*, *94*(C8), 10937–10954. https://doi.org/10.1029/JC094iC08p10937

Mesinger, F., DiMego, G., Kalnay, E., Mitchell, K., Shafran, P. C., Ebisuzaki, W., et al. (2006). North American Regional Reanalysis. *Bulletin of the American Meteorological Society*, *87*(3), 343–360. https://doi.org/10.1175/BAMS-87-3-343

National Ice Center (NIC) And NSIDC. (2010). Multisensor Analyzed Sea Ice Extent - Northern Hemisphere (MASIE-NH). NSIDC. https://doi.org/10.7265/N5GT5K3K

Niebauer, H. J. (1983). Multiyear sea ice variability in the eastern Bering Sea: An update. *Journal of Geophysical Research: Oceans*, *88*(C5), 2733–2742. https://doi.org/10.1029/JC088iC05p02733

Ólason, E. Ö., & Harms, I. (2010). Polynyas in a dynamic-thermodynamic sea-ice model. *The Cryosphere*, *4*(2), 147–160. https://doi.org/10.5194/tc-4-147-2010

Overland, J., & Pease, C. H. (1988). Modeling ice dynamics of coastal seas. *Journal of Geophysical Research: Oceans*, *93*(C12), 15619–15637. https://doi.org/10.1029/JC093iC12p15619

Paulson, C. A., & Simpson, J. J. (1977). Irradiance Measurements in the Upper Ocean. *Journal of Physical Oceanography*, *7*(6), 952–956. https://doi.org/10.1175/1520-0485(1977)007<0952:IMITUO>2.0.CO;2

Pritchard, R. S., Mueller, A. C., Hanzlick, D. J., & Yang, Y.-S. (1990). Forecasting Bering Sea ice edge behavior. *Journal of Geophysical Research: Oceans*, *95*(C1), 775–788. https://doi.org/10.1029/JC095iC01p00775

Reynolds, M., Pease, C. H., & Overland, J. E. (1985). Ice drift and regional meteorology in the southern Bering Sea: Results from MIZEX West. *Journal of Geophysical Research: Oceans*, *90*(C6), 11967–11981. https://doi.org/10.1029/JC090iC06p11967

Spreen, G., Kaleschke, L., & Heygster, G. (2008). Sea ice remote sensing using AMSR-E 89-GHz channels. *Journal of Geophysical Research: Oceans*, *113*(C2), C02S03. https://doi.org/10.1029/2005JC003384

Stabeno, P., Napp, J., & Whitledge, T. (2011a). Long-term observations on the Bering Sea shelf: ADCP data from mooring site 2. Version 1.0. UCAR/NCAR - Earth Observing Laboratory. https://doi.org/10.5065/D64Q7RZQ

Stabeno, P., Napp, J., & Whitledge, T. (2011b). Long-term observations on the Bering Sea shelf: biophysical mooring data from site 2. Version 1.0. UCAR/NCAR - Earth Observing Laboratory. https://doi.org/10.5065/D6JQ0Z15

Sullivan, M. E., Kachel, N. B., Mordy, C. W., Salo, S. A., & Stabeno, P. J. (2014). Sea ice and water column structure on the eastern Bering Sea shelf. *Deep Sea Research Part II: Topical Studies in Oceanography*, *109*, 39–56. https://doi.org/10.1016/j.dsr2.2014.05.009

Wang, J., Hu, H., Mizobata, K., & Saitoh, S. (2009). Seasonal variations of sea ice and ocean circulation in the Bering Sea: A model-data fusion study. *Journal of Geophysical Research: Oceans*, *114*(C2), C02011. https://doi.org/10.1029/2008JC004727

Woodgate, R. A., Stafford, K. M., & Prahl, F. G. (2015). A Synthesis of Year-Round Interdisciplinary Mooring Measurements in the Bering Strait (1990–2014) and the RUSALCA Years (2004–2011). *Oceanography*, *28*(3), 46–67. https://doi.org/10.2307/24861901

Zhang, J., Woodgate, R., & Moritz, R. (2010). Sea Ice Response to Atmospheric and Oceanic Forcing in the Bering Sea. *Journal of Physical Oceanography*, *40*(8), 1729–1747. https://doi.org/10.1175/2010JPO4323.1

Zhang, J., Woodgate, R., & Mangiameli, S. (2012). Towards seasonal prediction of the distribution and extent of cold bottom waters on the Bering Sea shelf. *Deep Sea Research Part II: Topical Studies in Oceanography*, *65*, 58–71. https://doi.org/10.1016/j.dsr2.2012.02.023

Zhang, J., Schweiger, A., Steele, M., & Stern, H. (2015). Sea ice floe size distribution in the marginal ice zone: Theory and numerical experiments. *Journal of Geophysical Research: Oceans*, *120*(5), 3484–3498. https://doi.org/10.1002/2015JC010770

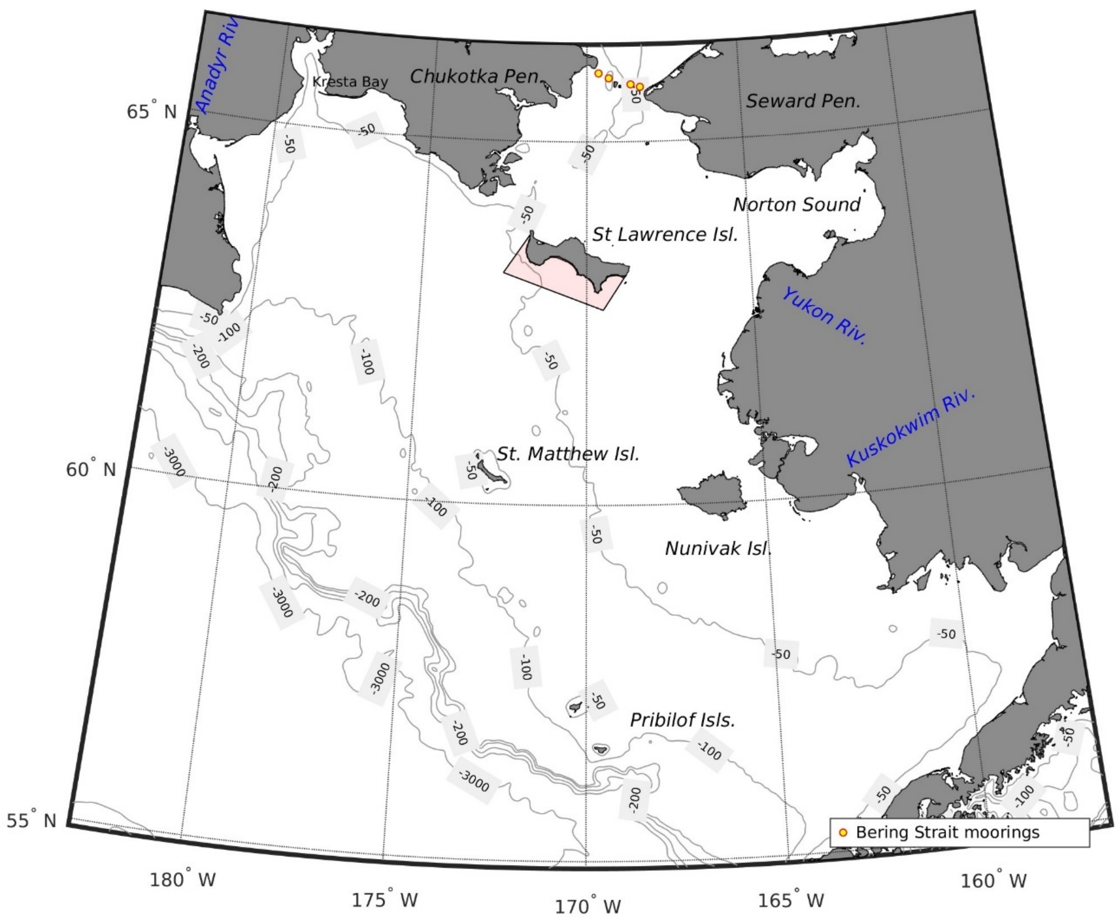

Figure 1. A map of the northern portion of model domain with mooring locations. Pink shaded area indicates region used for model-observation comparison of St. Lawrence polynya. The full model domain is displayed in Figure 1 of Durski et al.*(2016)*

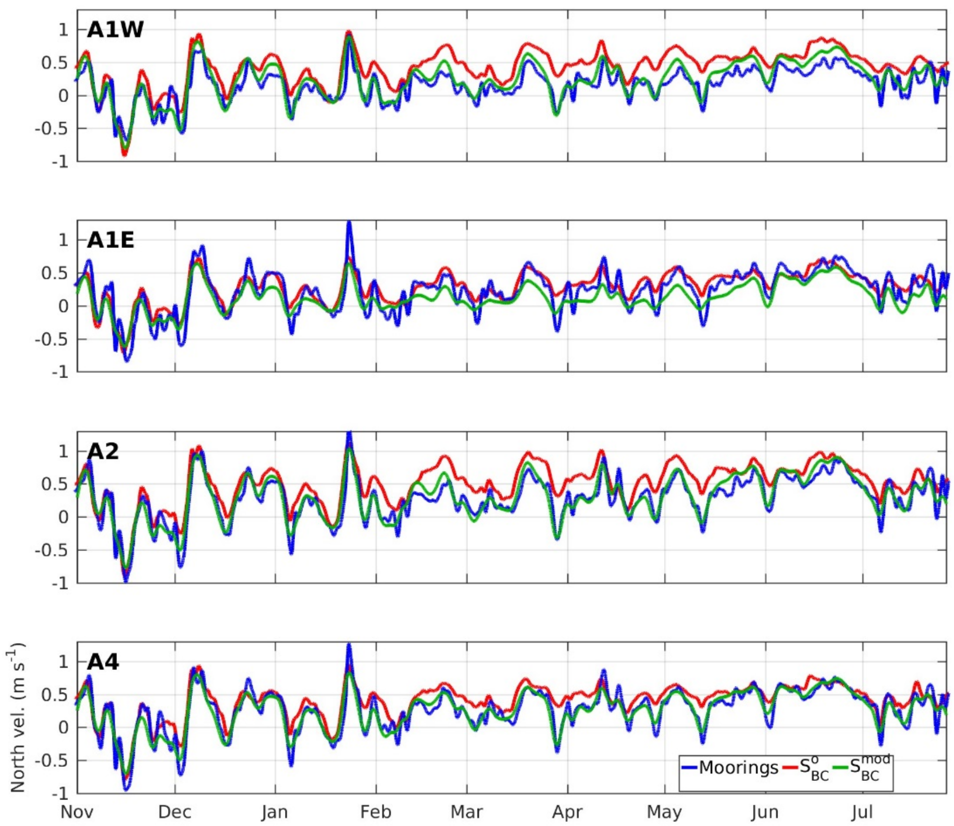

Figure 2. 2-day-filtered northward velocity at mid-depth in the Bering Strait at four mooring locations. Blue lines indicate the mooring measurements between November 2009 and August 2010, red line the model simulation before modifying the northern boundary condition and green lines indicate model results after modification. The longitudes of the mooring locations, depicted in Fig. 1, are (A1W, 169.28°W), (A1E, 169.62°W), (A2, 168.56°W) and (A4, 168.26°W).

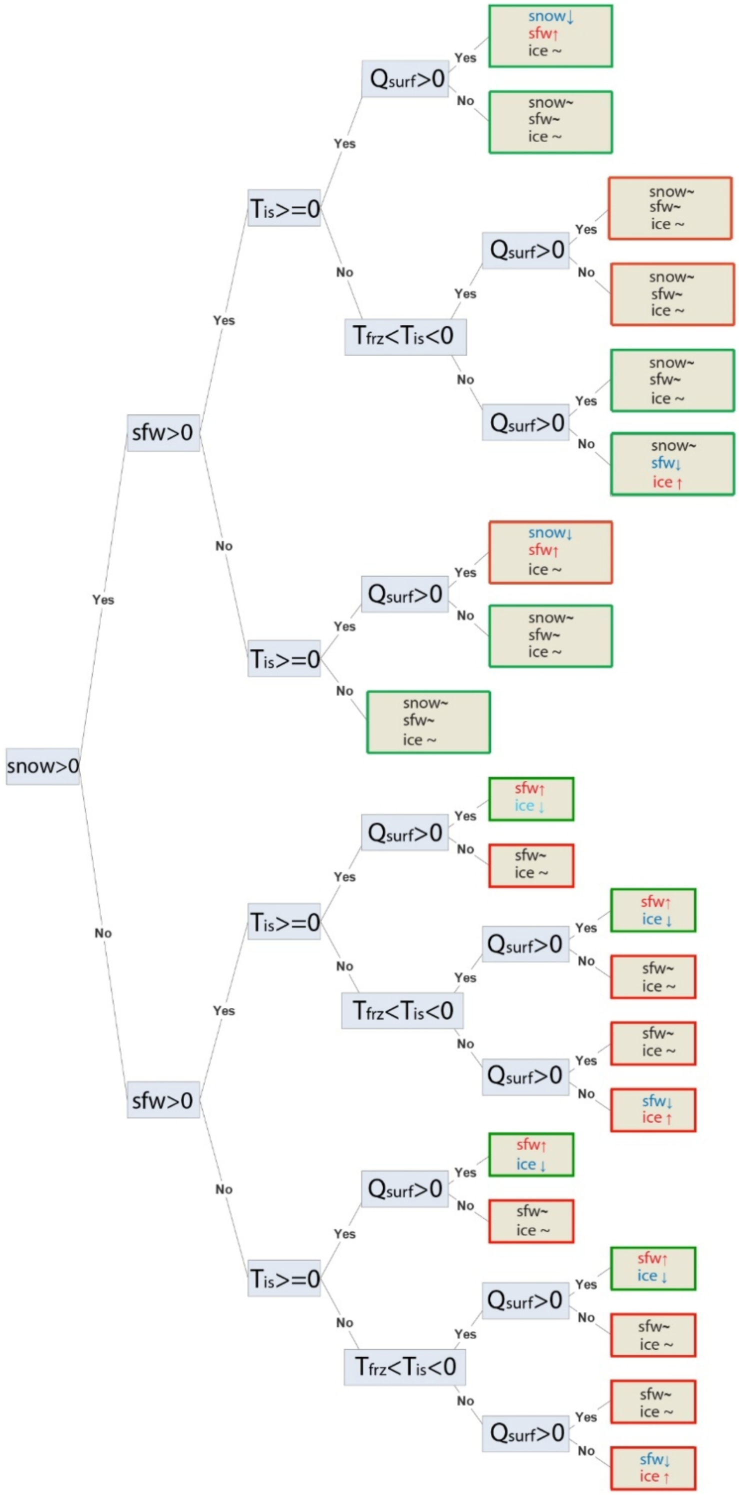

Figure 3. Decision tree for determination of the affected change in snow melt (h_{snow}=snow), meltwater ponds (h_{sfw} =sfw) and ice volume (h_i=ice) as a function of surface conditions. In the leaf nodes, text in red indicates a tendency to increase the variable, blue indicates a decrease, and black indicates no change. Red leaf node boxes indicate cases that were added or modified in our ice model formulation.

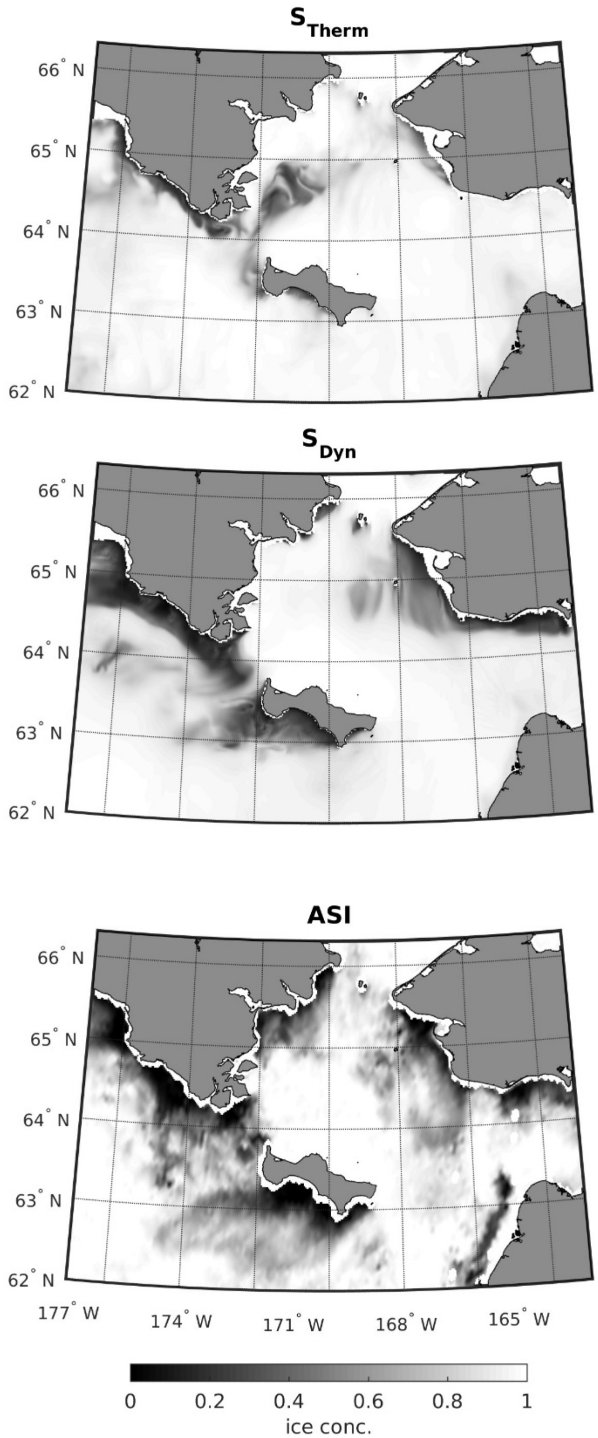

Figure 4. Comparison of ice concentration in the northern Bering Sea area centered on St. Lawrence Island on February 2nd 2010, from two simulations and a satellite derived product (ASI). S_{Dyn} includes modifications to the atmosphere-ice and ice-ocean drag coefficients and the ice strength relative to S_{Therm}.

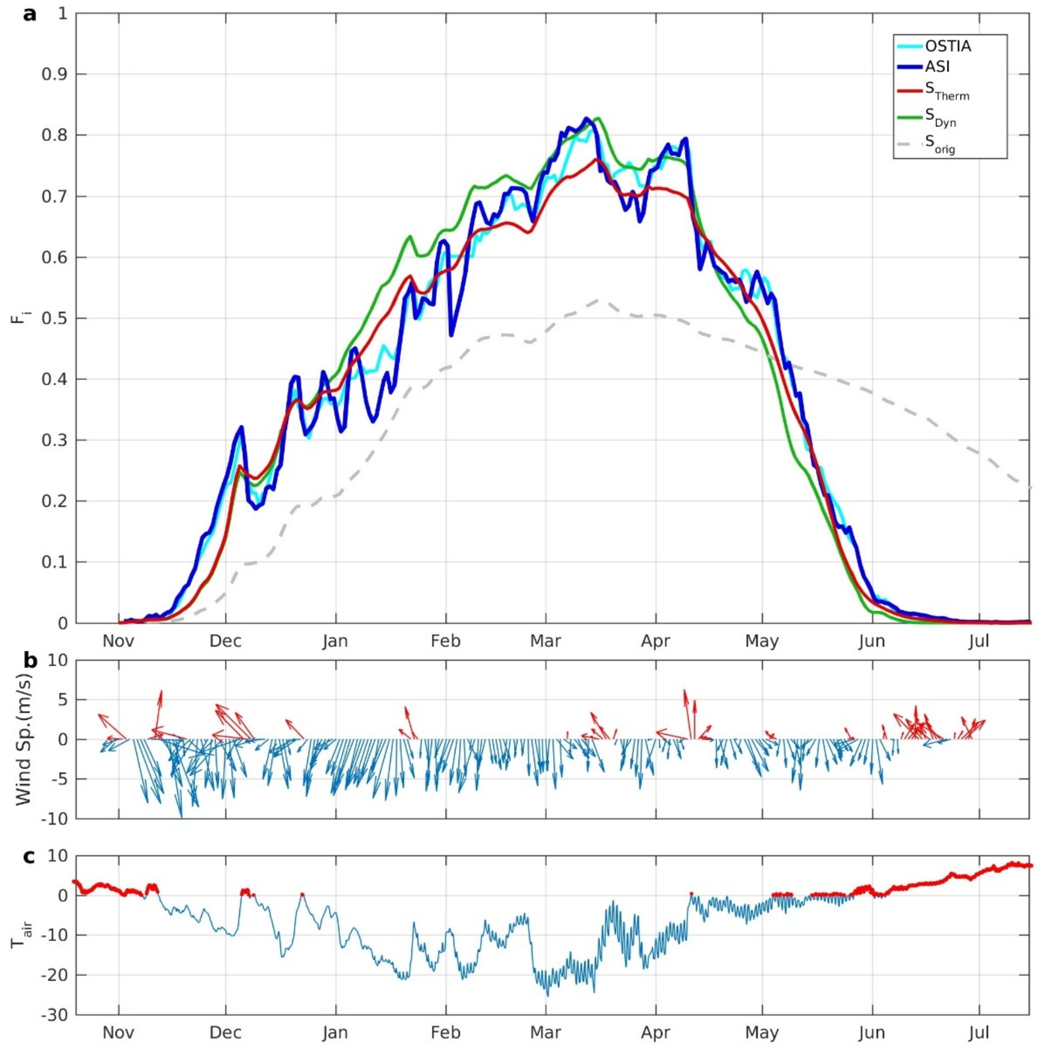

Figure 5. **a** Fraction of Eastern Bering Sea shelf covered in ice, (16), as a function of time for two model simulations with ice model modification, the two satellite estimates and for a simulation using the ice model in its original form. **b** Shelf-averaged wind velocity vectors from NARR (red arrows indicate a northward wind component). **c** Shelf-averaged surface(2m) air temperature from NARR (red line segments indicate times when the air temperature was above 0°C).

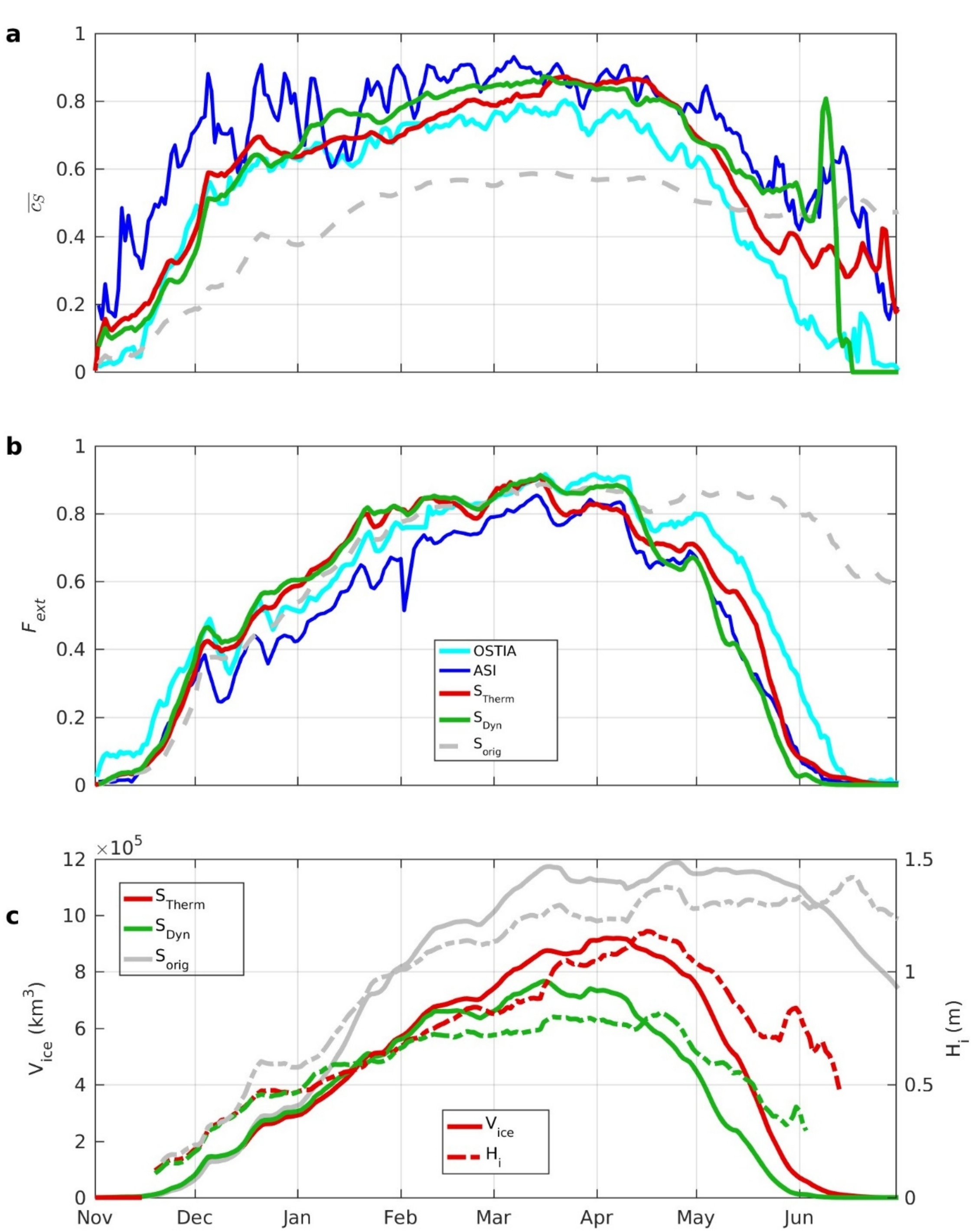

Figure 6. Comparison between simulations and satellite observations for **a** Average ice concentration per grid cell, (17), as a function of time, **b** the fraction of shelf grid cells that contain ice, (18), as a function of time and **c** the total ice volume (solid lines) and average ice thickness (dashed lines) for the two simulations. The average ice thickness is only plotted for times where the ice volume exceeds $1 \times 10^4 km^3$.

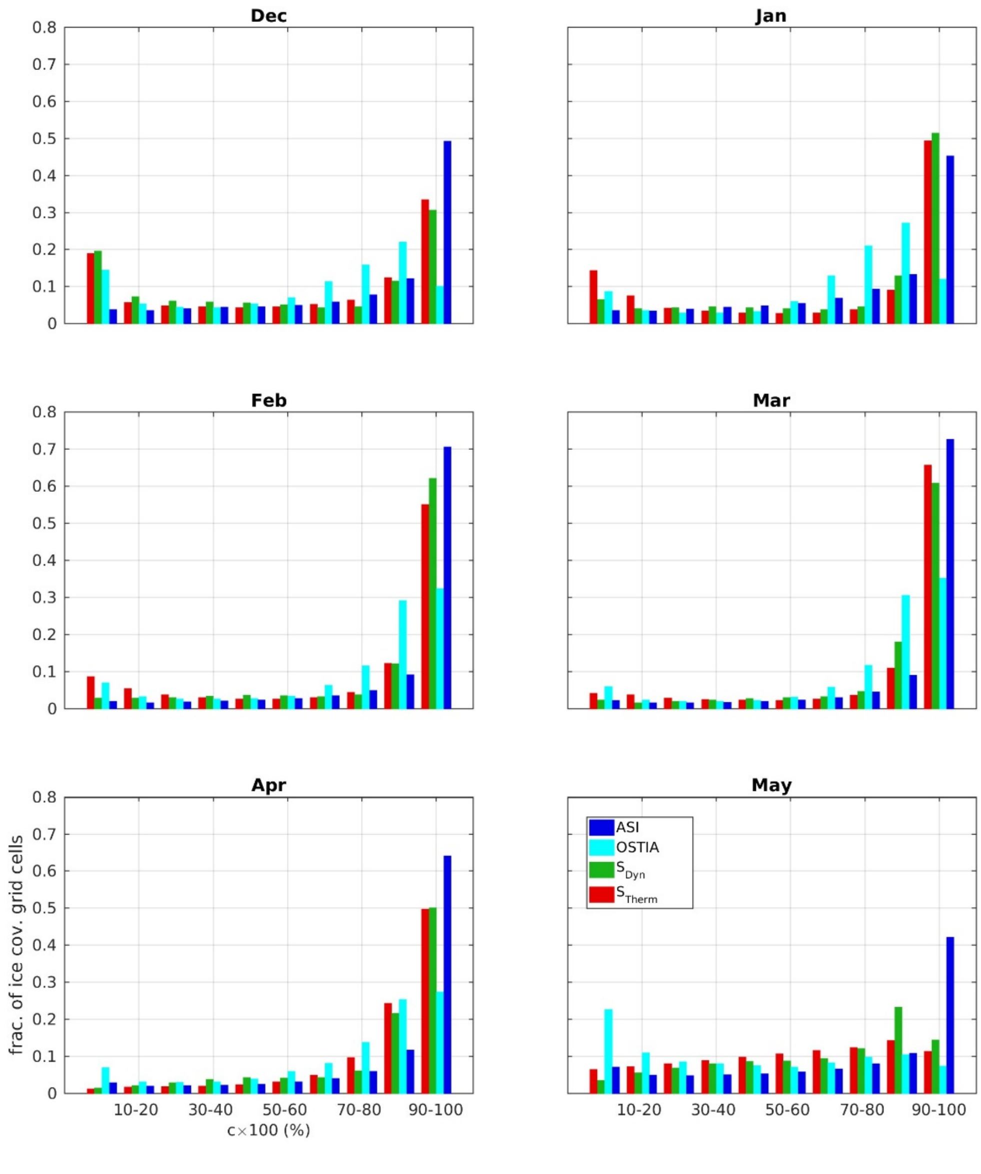

Figure 7. Monthly histograms of the ice concentration probability distribution from two satellite estimates and from the two simulations. Ice concentration is binned in 10% intervals.

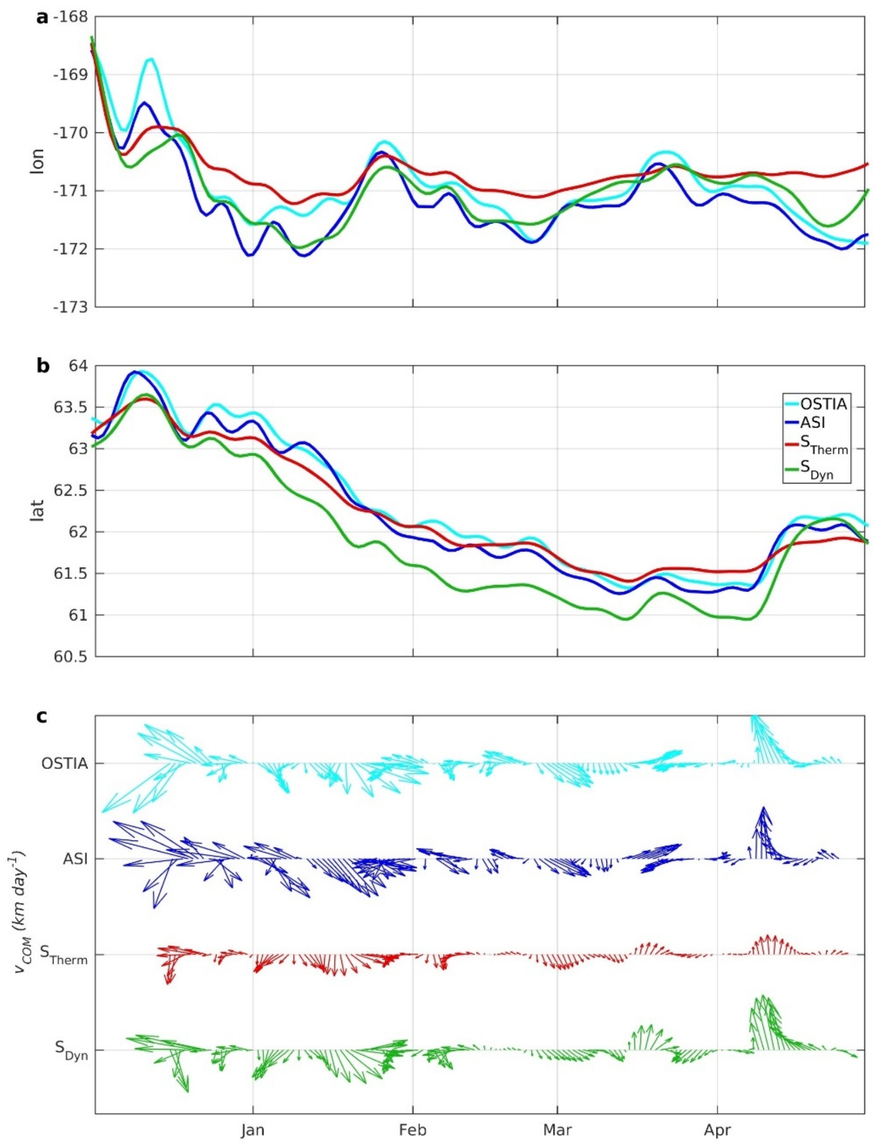

Figure 8. Comparison of the position of the two-dimensional center of mass of the ice concentration between the two ROMS simulations and the satellite estimates. Center of mass position has been filtered with a 3-day low-pass filter. Top two panels (**a** and **b**) show the longitude and latitude of the two-dimensional center of mass as a function of time. Bottom panel shows the magnitude and direction of movement of the time-filtered center of mass position as a function of time. Estimates from different products are offset vertically from each other by 30 m/s. .

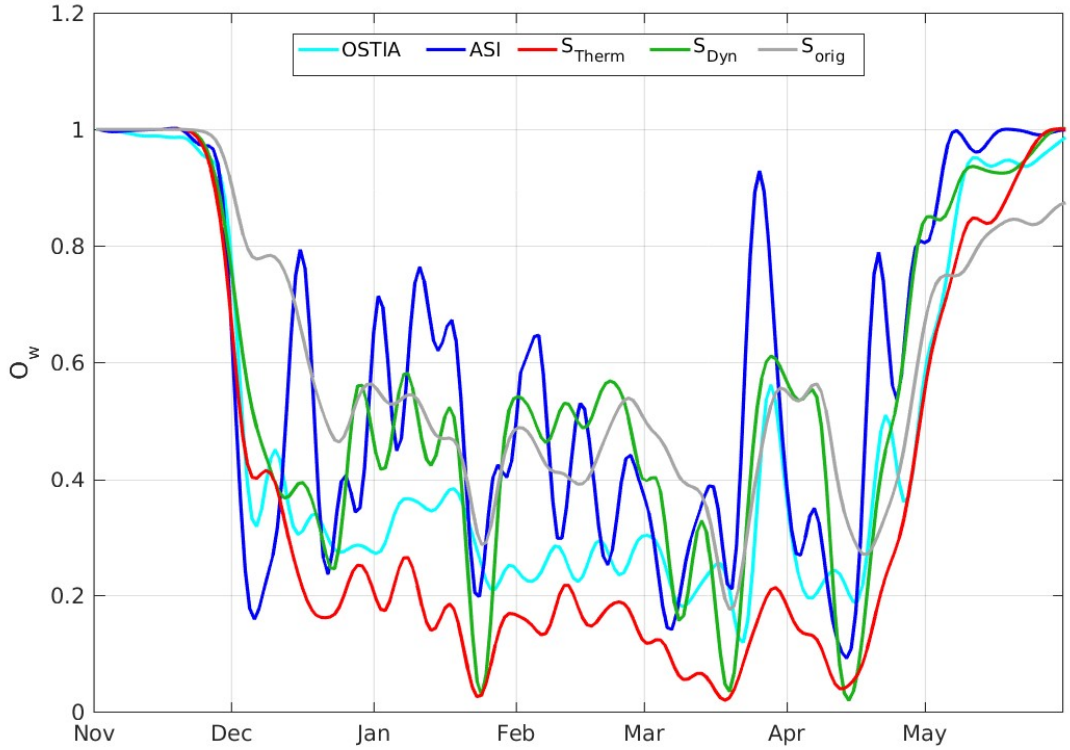

Figure 9. Comparison of the open water area south of St. Lawrence Island (pink shaded region in Figure 1) as a function of time from satellite estimates and simulations. Time series are filtered with a 3-day low-pass filter.

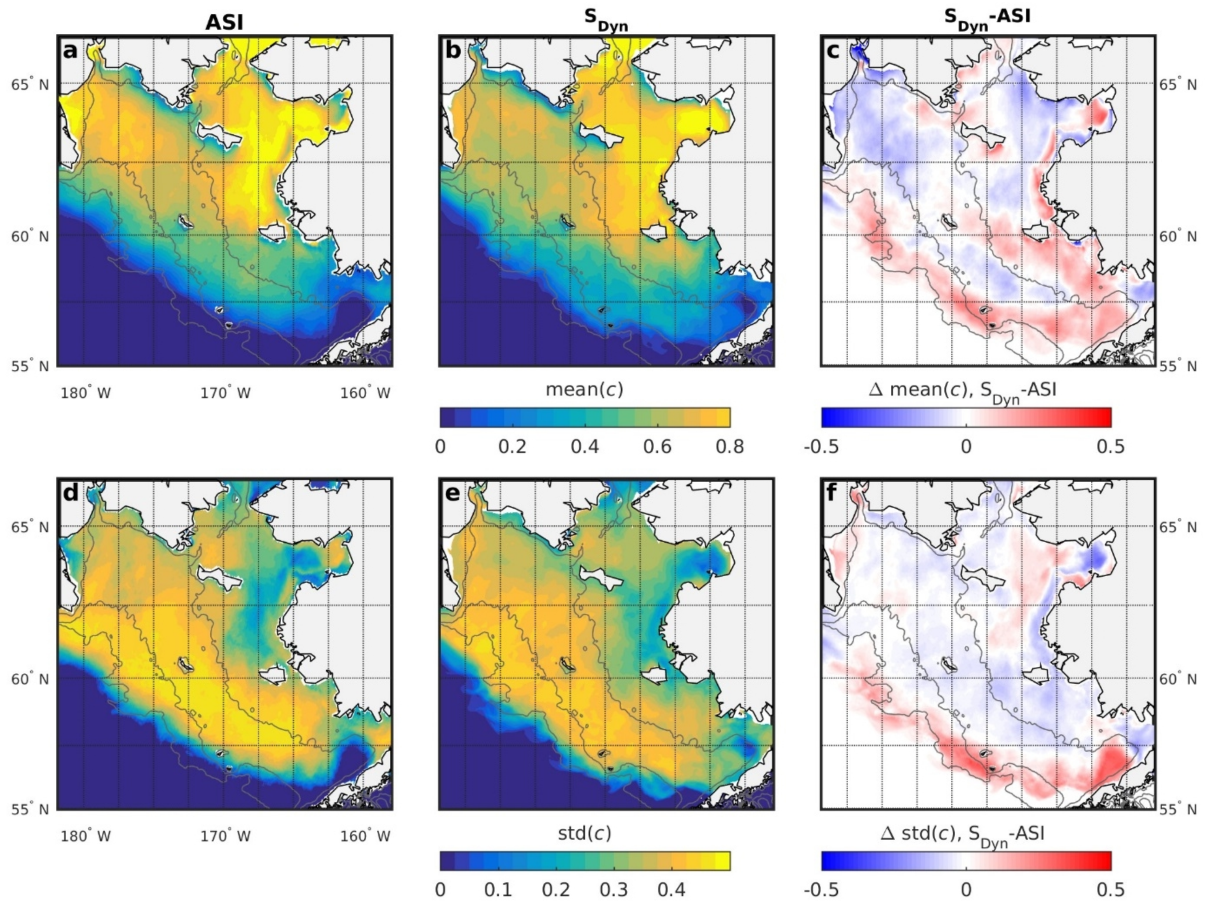

Figure 10. Comparison of ice concentration statistics between S_{Dyn} and the ASI satellite estimate. Panels **a** and **b** show the seasonal average ice concentration between December 2009 and May 2010, for ASI and S_{Dyn}. Panel **c** displays the difference between the two. Panels **d** and **e** show the standard deviation in ice concentration over the same period. Panel **f** shows the difference in the standard deviation between the model and satellite estimate. In each panel the -150m, -100m and -50m isobaths are contoured.

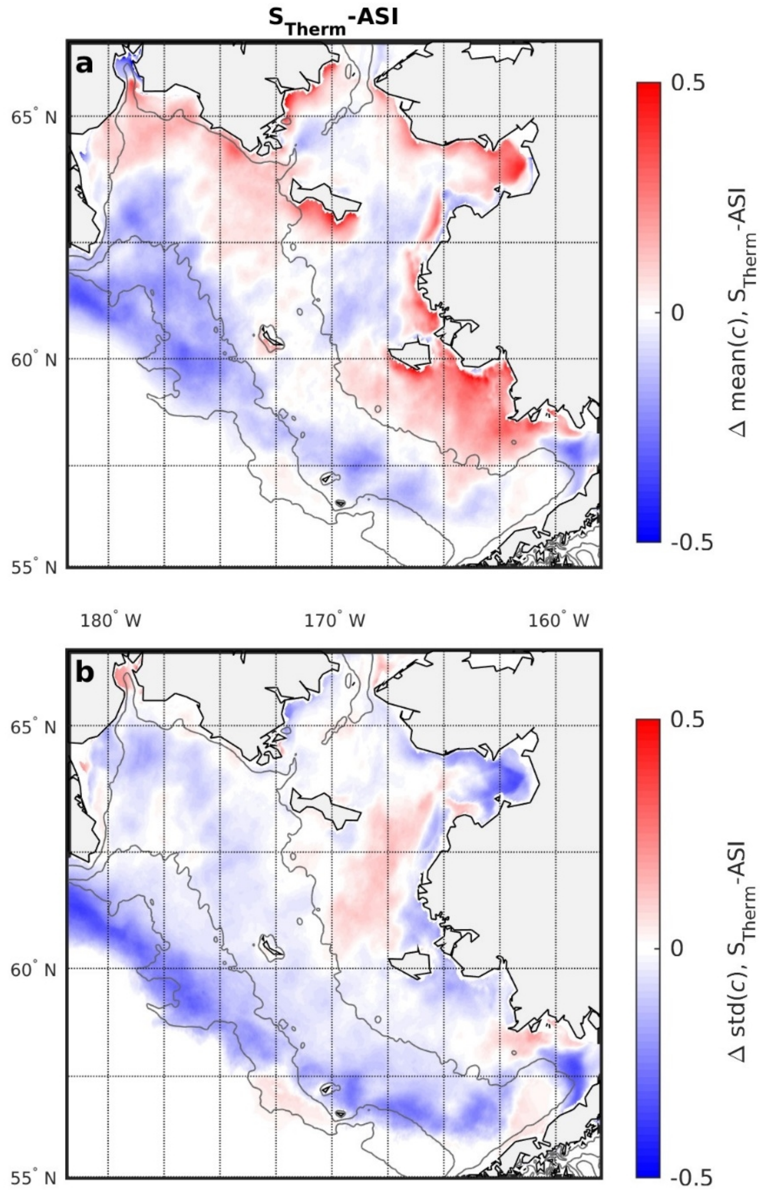

Figure 11. Comparison of ice concentration statistics between S_{Therm} and the ASI satellite estimate. Panel **a** displays the difference between the seasonal mean in the S_{Therm} simulation and the ASI estimate. Panel **b** displays the difference in the seasonal standard deviation between the simulation and satellite estimate. In each panel the -150m, -100m and -50m isobaths are contoured.

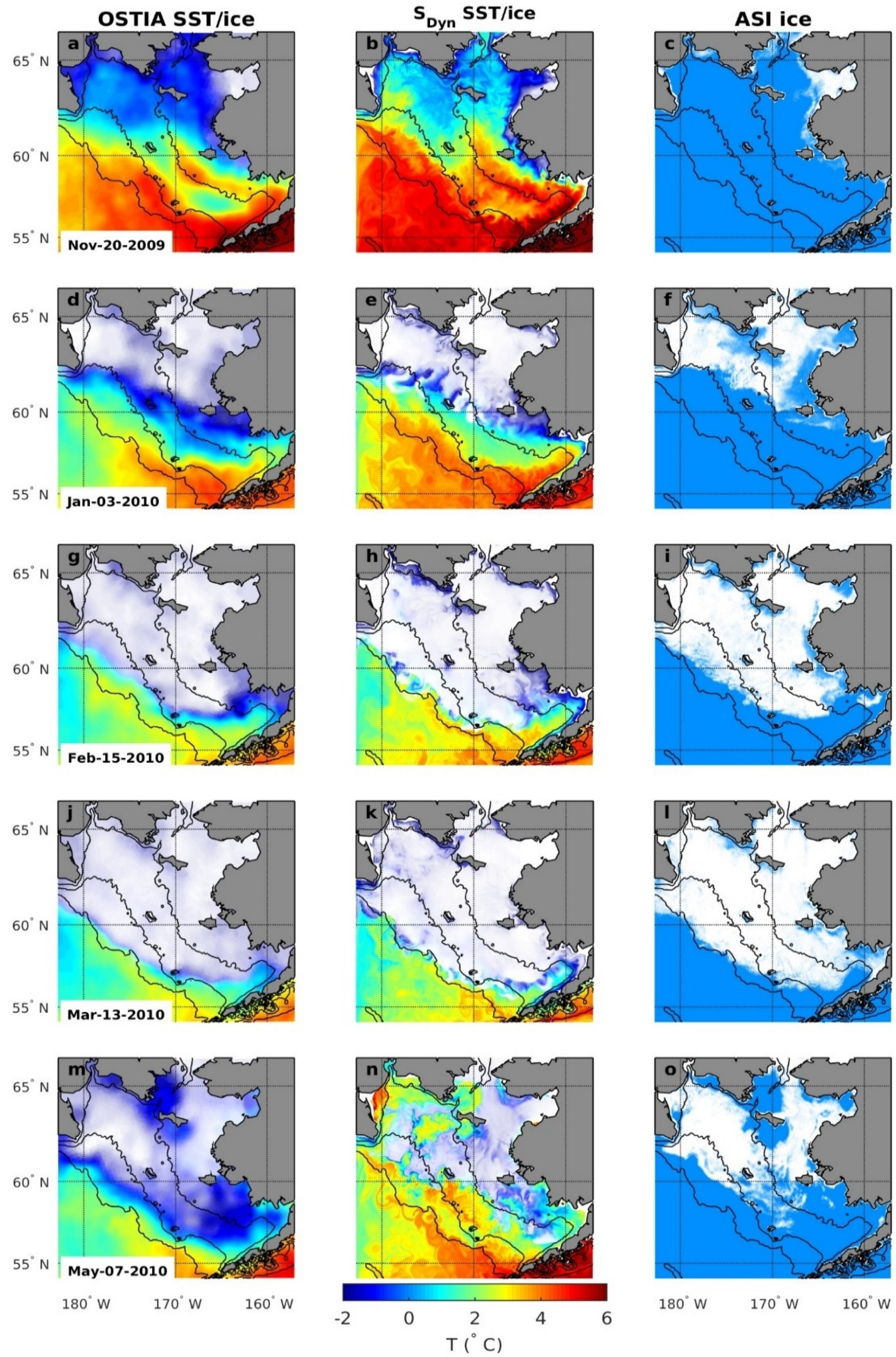

Figure 12. Comparison of ice coverage and SST for 5 different days over the winter season, for OSTIA (left column) and S_{Dyn} (middle column). SST is displayed in color, while the ice coverage is indicated with a transparency mask (white indicating 100% ice coverage and no masking, indicating 0% ice coverage). The right column shows the ASI estimate of ice concentration (this product does not produce an estimate for SST, so the background color is specified as blue). In each panel the -150m, -100m and -50m isobaths are contoured.